Probing and controlling magnetic states in 2D layered magnetic materials

Kin Fai Mak[1,2,3]*, *Jie Shan*[1,2,3]* and *Daniel C. Ralph*[1,3]*

Abstract | The discovery of atomic monolayer magnetic materials has triggered significant interest in the magnetism/spintronics and 2D van der Waals materials communities. Here we review recent progress in this rapidly growing field. We survey the physical properties of the large class of layered magnetic materials, and discuss recent advances in the study of these materials in the 2D limit. We then overview the optical and electrical techniques used for probing 2D magnetic materials (for reading their magnetic states) and the mechanisms for reorienting and/or switching 2D magnets by electric fields (for writing). Emerging device concepts based on magnetic van der Waals heterostructures are also discussed. We conclude with the future challenges and opportunities in this area of research.

Stimulated by the discovery of graphene[1] 15 years ago, scientists have greatly expanded the list of 2D layered materials, which cover almost all functionalities of solid-state systems including insulators, semiconductors, semimetals, metals and superconductors[2]. All of these electronic states can occur, for example, just within the family of 2D transition metal dichalcogenides[3]. Although there have been efforts to induce magnetism in graphene[4] and transition metal dichalcogenides[5–7], 2D materials with intrinsic magnetism had been missing until quite recently. There had been theoretical predictions of stable monolayer magnetic materials[8–14], but the first unambiguous experimental demonstrations of 2D layered magnets were reported only in 2017 (REFS[15,16]). The discovery of monolayer magnetic materials is generating considerable excitement within both the magnetism/spintronics and 2D materials communities because it enables fundamental studies of magnetism in the true 2D limit and applications based on the integration of 2D magnetic layers into device structures.

Within the magnetism/spintronics community, one reason why 2D magnetic materials are exciting is their potential to enable improved efficiency in the electrical control of magnetic devices. The most efficient mechanisms for controlling magnetic elements electrically are interface based, for example, spin-transfer torques and voltage-controlled magnetic anisotropy[17], so that they become increasingly efficient for thinner layers. Truly 2D magnets should therefore enable studies of the ultimate performance of these mechanisms, and of new mechanisms unique to 2D materials, such as those based on magnetoelectric and doping effects (see switching 2D magnets by electric fields section below). A detailed comparison between the physical properties of 2D and 3D magnetic materials is shown in TABLE 1. The discovery of 2D magnetic insulators is particularly exciting, because obtaining high-quality ultrathin magnetic insulators by depositing 3D materials has so far proved difficult. Compared with magnetic metallic thin films, ultrathin magnetic insulators are desirable to provide lower magnetic damping, long spin-wave propagation lengths, reductions in Ohmic losses and unwanted current shunting, and the ability to decouple input and output stages in designs for magnetic logic[18–20]. Yet when low-damping 3D magnetic insulators like yttrium iron garnet are deposited by conventional methods to make ultrathin films, the magnetic quality is generally degraded by non-stoichiometries and two-magnon scattering caused by surface roughness[21]; and interfacial disorder may degrade the flow of spin current through the interfaces. It will be interesting to see whether the assembly of 2D magnets into van der Waals heterostructures with well-controlled stoichiometry and pristine interfaces[22] might offer a useful alternative for experiments requiring ultrathin insulating magnetic layers. In addition, 2D magnets may open a new regime of fundamental studies of magnetism in which thermal fluctuations play a more central role than in 3D materials[23].

From the perspective of the 2D materials community, 2D magnetic layers greatly expand the types of device functionalities that can be explored. Initial studies have already shown that 2D magnets can exert strong magnetic proximity effects on adjacent 2D semiconductors[24], providing a means to directly control their valley degree

[1]Department of Physics, Cornell University, Ithaca, NY, USA.
[2]School of Applied and Engineering Physics, Cornell University, Ithaca, NY, USA.
[3]Kavli Institute at Cornell for Nanoscale Science, Ithaca, NY, USA.
*e-mail: kinfai.mak@cornell.edu; jie.shan@cornell.edu; dcr14@cornell.edu

https://doi.org/10.1038/s42254-019-0110-y

Key points

- There is a large class of layered magnetic materials with unique magnetic properties, which provides an ideal platform to study magnetism and spintronics device concepts in the 2D limit.
- Magneto-optical and electrical probes are powerful techniques for probing or reading the magnetic states of these materials.
- Because these materials are atomically thin, their magnetic states can be effectively controlled or switched by external perturbations other than magnetic fields, such as electric fields, free carrier doping and strain.
- New materials concepts, such as magnetizing 2D semiconductors by magnetic proximity coupling, and new devices, such as spin tunnel field-effect transistors, are rapidly emerging.
- Although rapid progress has already been made, there are many opportunities and challenges remaining in this young field.

of freedom[25,26]. Looking forward, we expect the coupling between 2D magnets and 2D superconductors to lead to exotic superconducting states with unusual supercurrents[27]. Heterostructures that incorporate 2D magnets to break time-reversal symmetry may provide a route to generate and manipulate new topological materials[28]. Controlling the relative twist angle between magnetic bilayers and multilayers may provide a means to control their interlayer exchange interactions, possibly allowing magnetic moiré patterns that stabilize spatially non-uniform spin textures[29,30]. Two-dimensional layers can also realize a wide range of different interesting magnetic states beyond ferromagnetism, including antiferromagnets, quantum spin liquids[31] and possibly topological magnetic skyrmions[30,31], in a form that can be readily incorporated into functional devices, thereby allowing new ways to investigate and manipulate these states.

In this Review, we first provide a brief overview of various layered magnetic materials and their physical properties (see REFS[31–33] for more comprehensive reviews on this subject). We then discuss recent advances in the study of these materials in the 2D limit, with a focus on detecting and controlling magnetism and emerging device concepts. We conclude with a discussion of future challenges and opportunities. This Review article, with a particular focus on the physics of 'reading' and 'writing' different types of magnetic states, is complementary to other recent reviews on this subject[34–36], which discuss the discovery of 2D magnetic materials and their emergent applications.

Families of layered magnetic materials

There is a rich collection of layered magnetic materials covering a wide spectrum of magnetic properties. The majority can be divided into two broad families, namely, transition metal halides[31] (including both dihalides and trihalides) and transition metal chalcogenides[32,33] (including both binary and ternary compounds). In most cases, the transition metal element is from the 3*d* transition metal row in the periodic table. Many of these materials are semiconductors with bandgaps covering the near-infrared to the ultraviolet spectral range, whereas a few are metallic. In general, the transition metal cations in each monolayer material are arranged in either a triangular lattice structure (the transition metal dihalides) or a honeycomb lattice structure (the transition metal trihalides and the transition metal chalcogenides; see FIG. 1a). In most cases, the cations are bonded to non-magnetic anions in octahedral coordination. Stacking such monolayers on top of each other forms the bulk material. The interlayer van der Waals bonding is weak, and consequently different stacking polytypes (for example, monoclinic and rhombohedral stacking) can exist[31]. Sometimes different polytypes even coexist within a single bulk material[37].

Table 1 | **Comparison between 2D magnets and thin films of 3D magnetic materials**

Physical properties	2D	3D
Surface to volume ratio	Higher	Lower
	Easier to tune by external perturbations, such as gating	Harder to control by external perturbations
Heterostructure interfaces	van der Waals bonding with saturated bonds	Covalent and ionic bonding with surface dangling bonds, often with disorder from the deposition process
	Absence of lattice mismatch problem (allows coupling to any other functional 2D materials, and control of twist angles)	Lattice mismatch limits coupling to other materials
	Weaker interfacial coupling	Stronger interfacial coupling, such as magnetic proximity
Exchange interaction anisotropy	Highly anisotropic exchange interactions (in-plane exchange is significantly stronger than out-of-plane exchange)	Often more isotropic exchange interactions
Mechanical	Variable strain	Fixed strain
	Flexible and harder to break	Hard to deform and brittle
Critical magnetic fluctuations	Important	Unimportant
	Weakened magnetic order and usually lower transition temperatures	More robust magnetic order and usually higher transition temperatures
	May be possible to utilize critical fluctuations to manipulate spin states	Impractical to access the narrow critical region

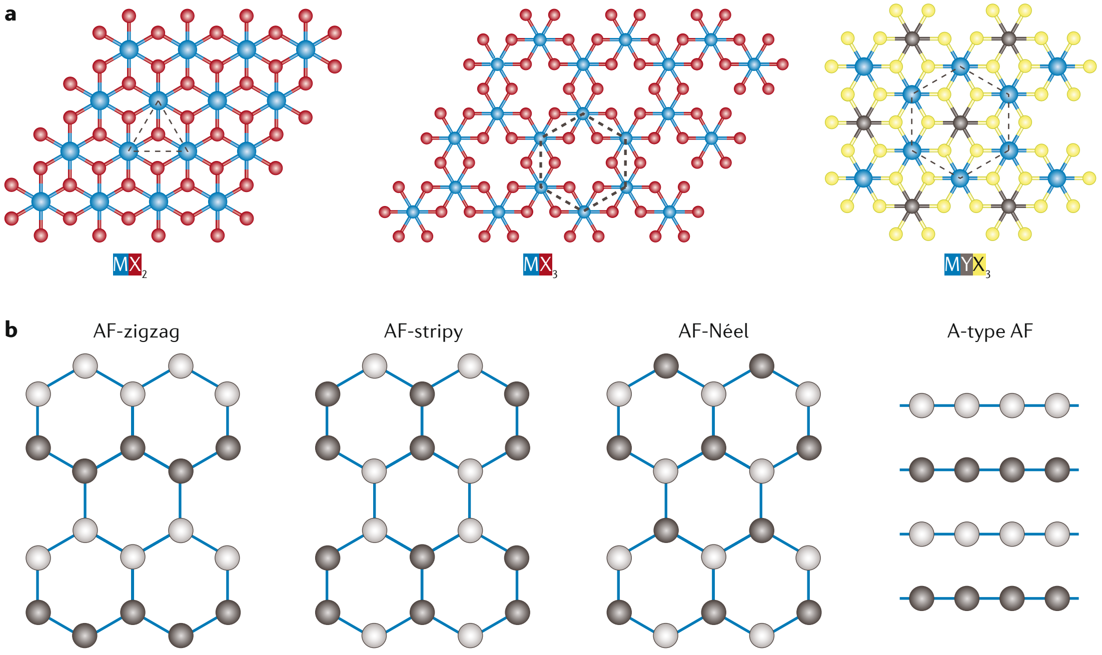

Fig. 1 | **Crystal structures and types of magnetic order for layered magnetic materials. a** | Crystal structures of monolayer transition metal dihalides (left), trihalides (middle) and ternary chalcogendies (right). M denotes 3*d* transition metal ions, X denotes halide (left and middle) and chalcogen (right) ions and Y denotes the element Si, Ge or P. The magnetic cations (blue) are arranged in a triangular lattice structure for the dihalides and in a honeycomb lattice structure for the trihalides and chalcogenides. The dashed lines denote the unit cells. **b** | Various types of antiferromagnetic (AF) order in layered magnetic materials (light grey and dark grey represent spin up and spin down, respectively). From left to right: intralayer AF-zigzag order, intralayer AF-stripy order, intralayer AF-Néel order and interlayer A-type AF order.

The magnetic moments in layered magnetic materials generally originate from the spin and orbital angular momenta of the 3*d* electrons in the transition metal cations. The crystal field from the octahedral coordination of the transition metal cations splits the five 3*d* orbitals into three low-energy t_{2g} levels and two high-energy e_g levels[38]. The valence electrons of the transition metal cations then fill these levels according to Hund's rules. For perfect octahedral coordination without spin–orbit coupling (SOC), the orbital magnetic moments are quenched and only spin magnetic moments need to be considered, giving a magnetic moment per transition metal atom of $\sim 2[S(S+1)]^{1/2}\mu_B$, where S is the total spin quantum number and μ_B is the Bohr magneton. With weak SOC compared with the crystal field splitting and the Coulomb energy, if the t_{2g} levels are half filled or fully filled, their orbital angular momenta sum to zero. However, with SOC and with a partial filling of the t_{2g} levels, the t_{2g} levels can provide a non-zero orbital angular momentum that contributes to the total magnetic moment[38,39] $g_J[J(J+1)]^{1/2}\mu_B$ (the orbital angular momenta of each e_g level remains quenched for weak SOC). Here J is the total angular momentum quantum number and g_J is the Landé g-factor. In the presence of lattice distortions from perfect octahedral coordination, orbital contributions to the total magnetic moment from all energy levels can be important.

Long-range magnetic ordering in layered magnetic materials is driven mainly by intralayer exchange interactions between the transition metal cations. Because of relatively large cation–cation distances, the direct exchange interaction between magnetic ions is weak. Instead, the super-exchange interaction, which is mediated by the non-magnetic anions between the magnetic cations, is the dominant interaction channel[8,10,11,40,41]. Both the sign and the magnitude of the super-exchange integral are sensitive to the cation–anion bond length and bond angle. Furthermore, theoretical studies[8,10,11] have suggested that not only the nearest-neighbour super-exchange interaction is important in these materials but also both the second-nearest-neighbour and the third-nearest-neighbour interactions can be significant. The interplay between these various channels of exchange interactions, together with the existence of magnetic anisotropy arising from the SOC, can give rise to a very rich variety of different magnetic states even in materials that have similar crystal structures. Below we provide a brief overview of the common types of magnetic states in these materials (TABLE 2) and discuss representative examples. We focus mainly on semiconducting spin systems. The interesting case of dilute magnetic layered topological insulators[42] will not be discussed in this Review owing to space limitations.

Ferromagnets. Ferromagnetic (FM) order exists in both layered transition metal halides[31] and chalcogenides[43], when the exchange interactions favour both intralayer and interlayer parallel spin alignments. The magnetic anisotropy is along the out-of-plane direction for all known cases. In general, these materials can be divided into two broad categories: localized-spin semiconductors and itinerant-spin metallic systems.

Table 2 | **Summary of layered magnetic materials**

Magnetic states	Chalcogenides	Dihalides	Trihalides
Ferromagnetic (spin systems)	$CrXTe_3$ (X = Si/Ge) [Cr^{3+} ($3d^3$)]	–	CrX_3 (X = Br/I) [Cr^{3+} ($3d^3$)]
Ferromagnetic (itinerant)	Fe_3GeTe_2 [Fe^{2+} ($3d^6$) and Fe^{3+} ($3d^5$)] Fe_xTaS_2 (Fe intercalated)	–	–
Antiferromagnetic (A-type)	$MnBi_2Te_4$ [Mn^{2+} ($3d^5$)]	FeX_2 (X = Cl/Br) [Fe^{2+} ($3d^6$)]	$CrCl_3$ [Cr^{3+} ($3d^3$)]
Antiferromagntic (C-type and G-type)	$MnPX_3$ (X = S/Se) (AF-Neel) [Mn^{2+} ($3d^5$)] MPS_3 (M = Fe/Co/Ni) (AF-zigzag) [Fe^{2+} ($3d^6$), Co^{2+} ($3d^7$) and Ni^{2+} ($3d^8$)]	–	–
Helimagnets	–	NiX_2 (X = Br/I) [Ni^{2+} ($3d^8$)] MnI_2 and CoI_2 [Mn^{2+} ($3d^5$), Co^{2+} ($3d^7$)]	–
Magnetoelectrics and multiferroics	$MnPX_3$ (X = S/Se) (magnetoelectrics)	FeX_2 (X = Cl/Br) (magnetoelectrics) NiX_2 (X = Br/I) (multiferroics) MnI_2 and CoI_2 (multiferroics)	$CrCl_3$ (magnetoelectrics)
Frustrated magnets	–	VX_2 (X = Cl/Br) [V^{2+} ($3d^3$)]	$RuCl_3$ [Ru^{3+} ($4d^5$)]

Examples of itinerant-spin systems include Fe_3GeTe_2 (REFS[44,45]) and Fe-intercalated 2H-TaS_2 (REF.[46]). For Fe_3GeTe_2, the magnetic Fe ions are arranged in a honeycomb lattice structure with two inequivalent Fe sites, whereas for Fe-intercalated 2H-TaS_2, they are situated in between the metallic TaS_2 layers. Examples of localized-spin systems include chromium ternary chalcogenides $CrXTe_3$ (X = Si or Ge)[43] and many-layered chromium trihalides $CrBr_3$ and CrI_3 (REF.[31]) (although in the few-layer limit CrI_3 can exhibit antiferromagnetic interlayer ordering). In both of these families of materials, the Cr^{3+} magnetic cations ($3d^3$) are arranged in a honeycomb lattice structure and bonded to non-magnetic anions in an octahedral coordination (FIG. 1a). Cr^{3+} cations are bonded to X^- anions for the trihalides[31] and each $X_2Te_6^{6-}$ anion is located at the centre of the Cr^{3+} honeycomb for the ternary chalcogenides[43]. The t_{2g} levels are half filled and the orbital moment is quenched. A spin-only magnetic moment of ~$3.9\mu_B$ per cation is thus obtained. Bandgaps for the localized-spin semiconductors range from the near-infrared to the near-ultraviolet spectral range[11,43].

Antiferromagnets. Antiferromagnetic (AF) layered materials have a rich variety of magnetic order[31–33] (TABLE 1). They can be broadly divided into two types[47]: those with intralayer FM order and interlayer AF order (the A-type), and others with intralayer AF order (the C-type and G-type). The latter can be further divided into AF-Néel, AF-zigzag and AF-stripy states[8,10] (FIG. 1b). Both out-of-plane and in-plane anisotropies and spin canting exist[31–33,48].

Examples of interlayer AF materials include $CrCl_3$ (REF.[49]), FeX_2 (X = Cl or Br)[50,51] and $MnBi_2Te_4$ (REF.[52]). $CrCl_3$ is a wide bandgap semiconductor with in-plane magnetic anisotropy[11,31]. It shares the same crystal structure and electronic configuration ($3d^3$) as $CrBr_3$ and CrI_3, but has a different magnetic structure — as noted above, few-layer CrI_3 is a layered antiferromagnet with out-of-plane magnetization[16] and $CrBr_3$ is a layered ferromagnet with out-of-plane spins[53], whereas few-layer $CrCl_3$ is a layered antiferromagnet with in-plane magnetic order[49]. In FeX_2, the magnetic Fe^{2+} cations ($3d^6$) are arranged in a triangular lattice structure and bonded to non-magnetic X^- anions[20] (FIG. 1a). Each Fe^{2+} cation carries $4t_{2g}$ and $2e_g$ electrons, giving rise to a spin-only magnetic moment of ~$4.9\mu_B$ with out-of-plane anisotropy[50]. Because of the partial filling of the t_{2g} levels, the orbital contribution to the magnetic moment (~10–20%) is not insignificant[35].

Examples of intralayer AFs include the rich family of transition metal thiophosphates MPS_3 (M = Mn, Fe, Co or Ni) and selenophosphates $MPSe_3$ (M = Mn, Fe or Ni)[32,33]. These materials share the same crystal structure as $CrSiTe_3$ and $CrGeTe_3$. Their electronic configurations are, however, different. In MPS_3 or $MPSe_3$, the transition metal ion M^{2+} only shares two electrons with the thiophosphate ($P_2S_6^{4-}$) or selenophosphate ($P_2Se_6^{4-}$) anion ($3d^5$ for Mn^{2+}, $3d^6$ for Fe^{2+}, $3d^7$ for Co^{2+} and $3d^8$ for Ni^{2+}). The spin-only magnetic moment of the M^{2+} cation depends on its electronic configuration (~$5.9\mu_B$ for Mn^{2+}, ~$4.9\mu_B$ for Fe^{2+}, ~$3.9\mu_B$ for Co^{2+} and ~$2.8\mu_B$ for Ni^{2+}). The orbital contribution (~30%) is important for Co and Ni compounds. Whereas $FePS_3$, $CoPS_3$, $NiPS_3$ and $FePSe_3$ display AF-zigzag order, $MnPS_3$ and $MnPSe_3$ have AF-Néel order[32,33,54]. The magnetic anisotropy is more complicated in the case of $FePS_3$, $FePSe_3$ and $MnPS_3$ which have out-of-plane anisotropy[32,33,54] ($MnPS_3$ has slightly canted spins[47]), and $NiPS_3$ and $MnPSe_3$, which have in-plane anisotropy[33,55].

Helimagnets. Due to the competition between in-plane FM and AF exchange, several layered magnetic materials develop a helimagnetic ground state, in which spins of neighbouring sites within a monolayer arrange themselves in a helical pattern[31]. Examples include NiX_2

(X = Br or I)[56,57], MnI_2 (REF.[58]) and CoI_2 (REF.[57]), whose crystal structure is identical to that of $FeCl_2$ and $FeBr_2$. For NiX_2, the Ni^{2+} cation ($3d^8$) supports fully filled t_{2g} levels and half-filled e_g levels and thus a spin-only magnetic moment of ~$2.8\mu_B$ per cation is expected. On cooling, these materials first undergo a transition into an A-type AF state with in-plane anisotropy, followed by another transition into the helimagnetic state, in which spin moments rotate within a monolayer with a temperature-dependent periodicity generally incommensurate with the lattice structure. The interlayer spins remain antiferromagnetically coupled in the helimagnetic state.

Magnetoelectrics and multiferroics. For some of the abovementioned materials in their magnetic ordered states, including bulk FeX_2 (X = Cl or Br)[50], NiX_2 (X = Br or I)[56,57], MnI_2 (REF.[58]), CoI_2 (REF.[57]), $MnPS_3$ (REF.[48]) and $CrCl_3$ (REF.[49]), both time-reversal and spatial inversion (structure plus spins) symmetries are simultaneously broken (although the combined operation of time-reversal inversion may still be a good symmetry). As a result, a linear magnetoelectric (ME) effect is allowed in these materials[59,60], in which an applied electric field can induce a sample magnetization linearly proportional to the applied field, and likewise an applied magnetic field can induce a linearly proportional polarization. This effect has attracted much attention in recent years because of its potential for realizing energy-efficient electric field control of magnetism for spintronics applications[61]. It is also relevant to topological physics as the ME susceptibility arises from non-zero Berry connections of the Bloch states[62]. Even in the absence of any applied fields, the rotating spin moments in helimagnetic systems, such as $NiBr_2$, NiI_2, MnI_2 and CoI_2, can induce a spontaneous electric polarization through SOC[56–58], making them multiferroics, meaning that magnetic and ferroelectric ordering coexist. Because one order induces the other, the coupling between magnetic moments and electric polarization is strong in these materials. Such strong coupling presents great opportunities for studies of electric field-controlled magnetism, especially in atomically thin materials, in which extremely large electric field can be applied in field-effect devices (discussed in Switching 2D magnets by electric fields section below).

Frustrated magnets. Two types of magnetic frustration are known for the transition metal halides, both of which suppress the magnetic ordering temperature (the temperature below which long-range magnetic order develops) substantially below the mean-field Weiss temperature (the temperature that reflects the exchange interaction energy scale)[20]. In the dihalides VX_2 (X = Cl or Br), the triangular lattice structure of the V^{2+} cations ($3d^3$) and the intersite AF exchange interaction gives rise to geometric frustration, which makes the AF ordering (120° Néel state) temperature much lower than the Weiss temperature[63]. In the trihalide $RuCl_3$, which has an AF-zigzag ground state[64], geometric frustration is absent for a honeycomb lattice of Ru^{3+} cations ($4d^5$). Instead, magnetic frustration originates from anisotropic exchange interactions that result from the much stronger SOC for $4d$ electrons compared with $3d$ electrons[65,66]. $RuCl_3$ has attracted attention because of its potential in realizing the Kitaev spin liquid model[67,68].

Theoretical background

The electronic structures of 2D layered magnets can be modelled by the Mott–Hubbard-type Hamiltonians, which include crystal field splitting, intersite hopping, and Coulomb and exchange interactions at the magnetic sites[40]. Ab initio methods have also been applied to calculate the electronic band structures[8–12,14,41,69]. Most of the materials are predicted to be Mott–Hubbard or charge-transfer insulators or semiconductors (except a few FM compounds), in good agreement with experiments. The conduction and valence bandwidths (determined by the intersite hopping) are narrow, significantly below 1 eV compared with a typical bandgap (determined by crystal field splitting and Coulomb repulsions) above 1 eV. The electronic structures of these materials in the 2D limit have not yet been actively investigated by spectroscopic methods.

The magnetic properties of the transition metal trihalides and ternary chalcogenides materials are generally well described by the Heisenberg model on a honeycomb lattice[8,10,41]. Values of the super-exchange integrals for specific materials are obtained from results from electronic structure calculations (from either the Hubbard-type Hamiltonian or ab initio methods)[8–12,14,41,69]. As noted above, it has been pointed out[8,10] that both the second-nearest-neighbour and the third-nearest-neighbour exchange couplings can be important in the determination of the magnetic ground state. Magnetic anisotropy energies and anisotropic exchange couplings can also be estimated from electronic structure calculations, and then included in the effective spin Hamiltonians[8]; shape anisotropy and interlayer magnetic field interactions are typically ignored in these theoretical models. The intralayer magnetic states predicted by such models are in reasonable agreement with experiments. Effects from the weak interlayer exchange coupling, however, are less explored. As we discuss in more detail below, recent theoretical results have suggested that the strength and sign of interlayer magnetic ordering might depend sensitively on the details of interlayer stacking[29,70].

In addition to predicting the magnetic ground state, spin Hamiltonians can also be used to calculate collective magnetic excitations[41,71,72] (for example, magnon dispersions), which provide important understanding for experimental studies of magnetic resonances[72–75], spin-wave excitations[76] and neutron scattering. Finite Berry curvature effects in the magnon dispersions and their consequences for anomalous magnon transport have also been investigated[71,77,78].

Experimental advances in 2D magnets

Early experiments on exfoliated layered magnetic materials used Raman spectroscopy to study few-layer transition metal ternary chalcogenides, such as AF $FePS_3$ (REFS[79,80]) and $RuCl_3$ (REF.[81]), and FM $CrSiTe_3$ (REF.[82]) and $CrGeTe_3$ (REF.[83]). Although Raman spectroscopy is a powerful probe of spin–lattice coupling[83] and collective magnon modes[84], it does not provide a direct measurement of the magnetic order parameter down to the monolayer limit. The use

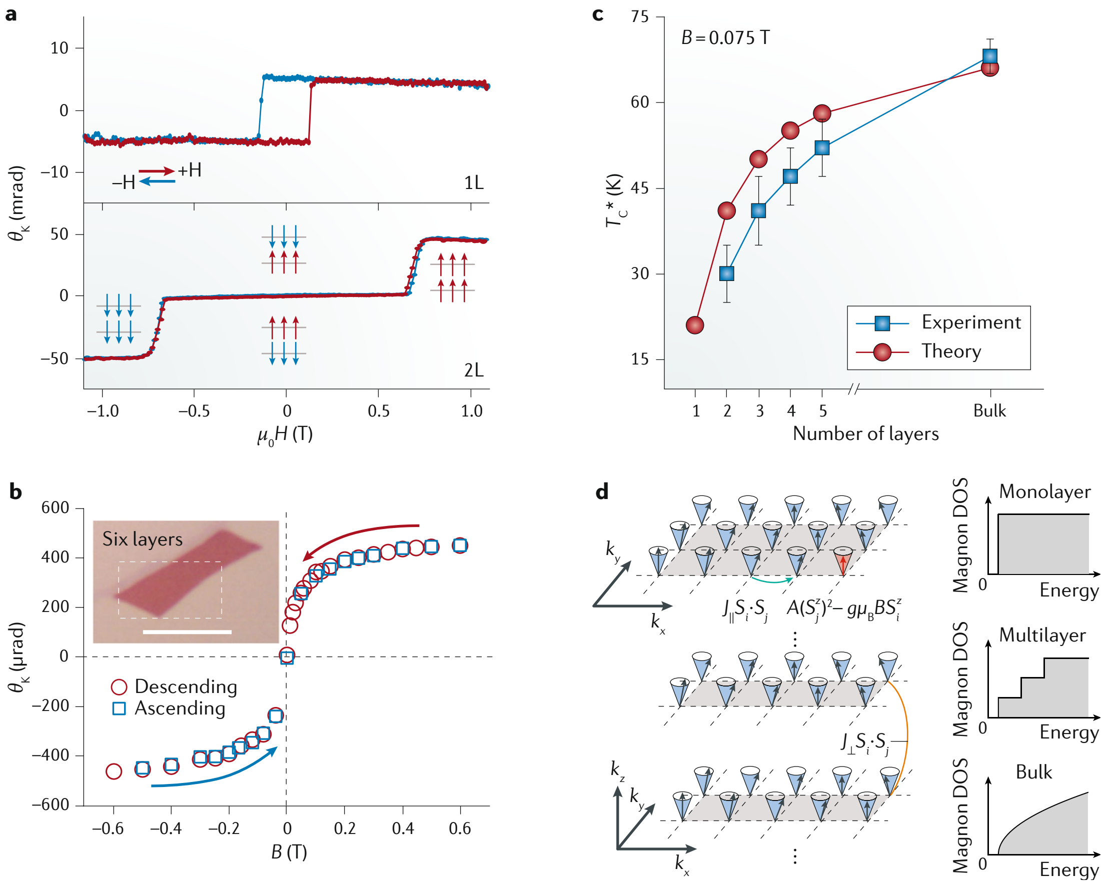

Fig. 2 | **Magneto-optical measurements of 2D magnetism. a** | External magnetic field (*H*) dependence of the magneto-optical Kerr effect (MOKE) angle θ_K for monolayer and bilayer CrI_3. The data show that monolayer (1L) CrI_3 is an intralayer ferromagnet with a coercivity of ~0.2 T (top), whereas bilayer (2L) CrI_3 is an interlayer A-type antiferromagnet exhibiting a spin-flip transition at ~0.7 T (bottom). The horizontal arrows represent the field scanning direction and the vertical arrows represent the spin orientation. **b** | Magnetic field (*B*) dependence of θ_K for few-layer $CrGeTe_3$. Blue and red correspond to forward and backward field scanning directions, respectively. Error bars are smaller than the symbols. The absence of hysteresis reflects the weaker easy-axis magnetic anisotropy compared with 2D CrI_3. The inset shows an optical image of the sample; the scale bar is 10 μm. **c** | Layer number dependence of the experimental and theoretical Curie temperatures (T_C^*) of 2D $CrGeTe_3$ for an out-of-plane magnetic field of 0.075 T. Error bars represent standard error. The decrease in Curie temperature originates from the effects of thermal magnon excitations in 2D. **d** | The low-energy magnon density of states (DOS) is larger in 2D $CrGeTe_3$ compared with 3D $CrGeTe_3$, making thermal excitations of low-energy magnons much easier, which significantly decreases the magnetic ordering temperature in 2D. The magnons are represented by the collective precessions of the spins *S* (arrows tracing out a cone). μ_0, permeability of free space; μ_B, Bohr magneton; *A*, single-ion anisotropy; *g*, spin *g*-factor; *i* and *j*, lattice site labels; $J_{\parallel}$, intralayer exchange coupling; $J_{\perp}$, interlayer exchange coupling; k_x, k_y and k_z are the *x*, *y* and *z* components of the magnon wavevector, respectively; superscript *z*, *z*-component of spins. Panel **a** is adapted from REF.[16], Springer Nature Limited. Panels **b–d** are adapted from REF.[15], Springer Nature Limited.

of other techniques to probe the magnetic order more directly was initially inhibited by difficulties in the preparation and preservation of monolayer magnetic samples, many of which degrade quickly in ambient conditions.

In 2017, two independent studies reported the use of the magneto-optical Kerr effect (MOKE) to measure the sample magnetization of ultrathin layered magnetic materials — for CrI_3 down to the monolayer limit[16] and for $CrGeTe_3$ down to bilayers[15]. In the study on CrI_3, the extremely air-sensitive material was prepared in an inert environment and then fully encapsulated between graphene protective layers for subsequent measurements. Interestingly, although previous measurements had shown that bulk CrI_3 is a ferromagnet below the Curie temperature $T_C \approx 60$ K (REF.[37]), bilayer CrI_3 is an A-type antiferromagnet similar to $FeCl_2$ and $FeBr_2$ (parallel spins within each layer with antiparallel alignment between layers). The bilayer material carries nearly zero magnetization under zero magnetic field and undergoes a spin-flip transition into the FM alignment for external magnetic fields above a critical field ~0.7 T (FIG. 2a). By contrast, monolayer CrI_3 is a ferromagnet with out-of-plane anisotropy. Theoretical studies have suggested that the observed layer-dependent magnetism originates from the locking of atomically thin samples in the monoclinic stacking order[29,70,85,86], in contrast to the stacking order of the bulk material, which changes from a high-temperature monoclinic stacking to a low-temperature rhombohedral stacking order[37]. The locking of the material in the monoclinic phase favours A-type

AF order over FM order. Structural characterizations of the stacking order of 2D $CrCl_3$ (REF.[87]) and CrI_3 (REF.[88]) support this claim. The correlation between the magnetic state and stacking order has been directly demonstrated by recent experiments on few-layer CrI_3 under hydrostatic pressure[89,90].

In the initial study on $CrGeTe_3$ (REF.[15]), the samples were exposed to air so that there could have been some degradation of very thin samples. Like the bulk material, the atomically thin samples remain FM down to the bilayer limit (FIG. 2b), although the transition temperatures are reduced from about 70 K in the bulk to below 30 K in bilayers (FIG. 2c). The reduced transition temperature in 2D has been ascribed to an increased excitation of magnons in the 2D limit, which tend to suppress long-range order (FIG. 2d). An enhancement of the transition temperature with increasing magnetic field was also observed, and analysed in terms of a field-enhanced magnetic anisotropy. This study concluded that the transition temperature in 2D $CrGeTe_3$ is determined by the magnon excitation gap, whereas the transition temperature in 3D $CrGeTe_3$ is more directly governed by the strength of exchange interactions. Future studies on encapsulated samples protected from air degradation will be helpful to further test these statements.

The observation of intrinsic magnetism in truly 2D materials might seem at odds with the Mermin–Wagner theorem[91], which implies that no finite-temperature long-range magnetic order can exist in 2D systems with fully isotropic and short-ranged exchange interactions between localized spins. However, since all real material systems possess certain degrees of magnetic anisotropy, the existence of 2D magnetic materials does not contradict the Mermin–Wagner theorem.

Following the initial experiments discussed above, tremendous progress has been made on the development of new 2D magnetic materials. Most notably, 2D ferromagnets with greatly enhanced transition temperatures (in some cases above room temperature) have been reported. For example, ionic gated few-layer Fe_3GeTe_2 exhibits FM order up to 310 K (REF.[44]). Ungated Fe_3GeTe_2 samples show FM transition temperatures suppressed as sample thickness decreases, from ~180 K in the bulk to ~20 K in the monolayer material. Epitaxial growth of 2D 1T-VSe_2 films on graphite and MoS_2 substrates has also been reported, with Curie temperatures above 350 K (REF.[92]). Interestingly, whereas bulk 1T-VSe_2 is paramagnetic without FM ordering, monolayer 1T-VSe_2 clearly shows FM ordering with in-plane anisotropy. The FM order disappears with increasing sample thickness, consistent with earlier theoretical predictions[13,93,94]. The reported large magnetic moment per V ion, however, requires further confirmation. FM order at room temperature has also been reported in monolayer 1T-$MnSe_2$ grown epitaxially on GaSe and on $SnSe_2$ (REF.[95]). The successful growth of monolayer ferromagnets with high transition temperatures using wafer-scale epitaxial methods has opened the door for large-scale spintronics applications using these materials.

Next we review the basic physics underlying the experimental techniques for probing the magnetic state in these materials and controlling the magnetic orientation (that is, the physics of reading and writing the magnetic state for potential technologies). Unique potential applications using vertical heterostructures based on these new materials are also discussed.

Optical measurement methods. Exfoliated samples of 2D magnets generally are limited to micrometre-scale sizes. Given their atomic-scale thicknesses, this means that the volumes of these samples are too small to provide measurable signals for most conventional magnetic probes, including neutron scattering, superconducting quantum interference device (SQUID) magnetometry (not including micro-SQUID or nano-SQUID) and vibrating-sample magnetometry. Instead, most recent research on 2D magnetic materials relies on optical and electrical methods to probe magnetic ordering. We briefly review the basic physics of these probes and their application.

Optical spectroscopy is a powerful non-contact method that can unambiguously distinguish various types of magnetic order with extremely high sensitivity and submicrometre resolution. As mentioned above, many of the early works on 2D layered magnetic materials used micro-Raman spectroscopy[79–84]. Although the technique is very useful in probing collective magnetic excitations, such as high-energy terahertz magnons[84] and spin-lattice coupling[83], it cannot unambiguously identify the type of magnetic order in most cases. Furthermore, because Raman scattering is a weak inelastic light-scattering process, probing magnetism in 2D magnetic materials with this technique requires long integration times. We therefore focus in this Review on more straightforward magneto-optic effects[96] that can directly probe the sample magnetization. In particular, we consider magnetic birefringence and dichroism, in which the measurable quantities are directly related to the complex optical conductivity ($\sigma = \sigma^{(1)} + i\sigma^{(2)}$, with $\sigma^{(1)}$ and $\sigma^{(2)}$ denoting the real and imaginary parts, respectively) of the material[97,98]. Other emerging techniques such as scanning nitrogen vacancy microscopy[99] will not be covered here.

The most commonly used magneto-optic effects to investigate 2D magnets are based on magnetic circular birefringence and dichroism[96–98] (FIG. 3). Magnetic circular birefringence probes the difference in optical refraction between left-circularly and right-circularly polarized light in response to sample magnetization M. This difference is determined by magnetization-dependent contributions to the imaginary part of the complex optical conductivity $\sigma^{(2)}$. The related effect of magnetic circular dichroism (MCD) probes the difference in absorption between left-circularly and right-circularly polarized light, as determined by the real part of the optical conductivity $\sigma^{(1)}$. In the basis of linearly polarized light (with electric field E_x and E_y) propagating along the z direction, these effects originate from the antisymmetric off-diagonal elements in the complex optical conductivity tensor $\sigma_{xy} = -\sigma_{yx} \propto M$, which are dependent on the sign of M (analogous to the anomalous Hall effect (AHE) in electrical transport)[97,98]. As a result of explicit time-reversal symmetry breaking, the effect is also non-reciprocal[100]. When the circular polarization basis ($E_x \pm iE_y$) is used, the complex optical conductivity tensor becomes diagonal $\sigma = \begin{pmatrix} \sigma_+ & 0 \\ 0 & \sigma_- \end{pmatrix}$, in which the

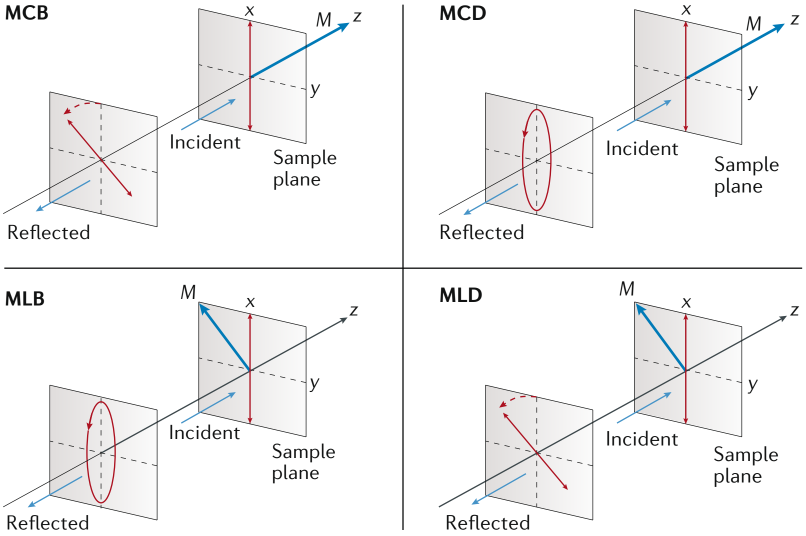

Fig. 3 | **Magneto-optical birefringence and dichroism.** Schematic of various modes for magneto-optical measurements in the reflection geometry. The light blue arrows represent the incident and the reflected light propagation directions. The blue arrow shows the magnetization (*M*) direction of the sample. The red solid lines and arrows represent the light polarization state. The red dashed lines and arrows denote rotation of polarization. Magnetic circular birefringence (MCB) and magnetic circular dichroism (MCD) probe the antisymmetric part of the off-diagonal elements of the optical conductivity tensor. Magnetic linear birefringence (MLB) and magnetic linear dichroism (MLD) probe the difference in the optical conductivities parallel and perpendicular to the sample magnetization. Birefringence and dichroism are related to the imaginary and the real parts of the optical conductivities, respectively.

different responses to left-circularly and right-circularly polarized light become explicit[97,98].

There are different experimental schemes to carry out magnetic circular birefringence or dichroism measurements. One is to measure changes in the polarization rotation angle for linearly polarized incident light (FIG. 3), such as in the Faraday rotation and MOKE measurements[101]. The rotation angle is proportional to the difference in the imaginary conductivity $\theta \propto \sigma_+^{(2)} - \sigma_-^{(2)}$ (REFS[97,98]). MOKE experiments can be further subdivided into polar MOKE, longitudinal MOKE and transverse MOKE depending on the light propagation direction with respect to the magnetization direction[102]. Another option is to measure changes in the ellipticity of the polarization for the reflected or transmitted light, as in MCD measurements[101]. The ellipticity is determined by differences in the real part of the conductivity, $\epsilon \propto \sigma_+^{(1)} - \sigma_-^{(1)}$ (see REFS[97,98] and FIG. 3). MCD experiments can also be carried out directly in the circular polarization basis by measuring the absorption difference between left-circularly and right-circularly polarized incident light.

Due to their sensitivity to *M*, MOKE and MCD microscopy can be used most straightforwardly to probe 2D magnetic materials in which the intralayer spins are ordered ferromagnetically. The results of polar MOKE measurements for monolayer CrI_3 and few-layer $CrGeTe_3$ (REFS[15,16]) are shown in FIG. 2a,b. A typical FM behaviour is seen in CrI_3, with clear magnetic hysteresis and a large remanent magnetization at zero applied magnetic field. The $CrGeTe_3$ sample can also display hysteresis, but with a more-rounded transition and less remanence, reflecting a much weaker magnetic anisotropy in this material compared with CrI_3. Subsequent MCD measurements using circularly polarized light as the basis have shown similar results for CrI_3 (REFS[103–105]).

We make a few comments on the strengths and weaknesses of these techniques. First, it is advantageous to use the circularly polarized light basis in MCD measurements because there is no significant diamagnetic background from optics (for example, the objective lens) in magnetic field-dependence studies. The reason is that typical optical elements are transparent, $\sigma_+^{(1)} \approx \sigma_-^{(1)} \approx 0$, in the near-infrared to near-ultraviolet spectral range so that they do not contribute to MCD signals. No background subtraction is therefore needed. By contrast, for MOKE measurements, optical elements subject to a magnetic field generally have a non-zero magnetic circular birefringence, so a background subtraction is typically required. Second, as a result of the multilayer structure of samples on SiO_2/Si substrates, the real and the imaginary part of the sample's optical conductivity are generally mixed in both the MOKE and MCD measurements[106,107]. Care is needed to extract quantitative values of the optical conductivities for individual layers within the sample stack. Third, existing results for both MOKE and MCD clearly demonstrate enough sensitivity to detect magnetic moments from a single layer of spins. This is in fact not surprising given the signal level of ~10 mrad for a monolayer ferromagnet and the typical measurement noise down to 100 nrad $Hz^{-1/2}$ (REF.[100]). Signal levels might be enhanced even further by selecting probe wavelengths at resonance with the optical transitions of the materials. However, so far, MOKE and MCD spectroscopy on 2D magnets has not been studied systematically.

An immediate question is whether MOKE and MCD can be applied to probe 2D AF states. Although the net sample magnetization is zero in AF materials, it has been shown theoretically that antisymmetric off-diagonal conductivity elements $\sigma_{xy} = -\sigma_{yx}$ can be non-zero for antiferromagnets with broken $\mathcal{T}\mathcal{I}$ (REFS[59,60,69,108]) and/or $\mathcal{T}\mathcal{M}$ (REF.[109]) symmetries. Here $\mathcal{T}\mathcal{I}$ is the combined time-reversal ($\mathcal{T}$) and inversion ($\mathcal{I}$) operations, and $\mathcal{T}\mathcal{M}$ is the combined $\mathcal{T}$ and mirror ($\mathcal{M}$) operations. In fact, the importance of $\mathcal{T}\mathcal{I}$ symmetry in antiferromagnets has been well documented in the literature of magnetoelectrics[59,60,108], in which both $\mathcal{T}$ and $\mathcal{I}$ symmetries are broken, but combined $\mathcal{T}\mathcal{I}$ is often a good symmetry (see switching 2D magnets by electric fields sectionbelow). In such cases, the application of an external electric field, which breaks the $\mathcal{T}\mathcal{I}$ symmetry, can induce a sample magnetization in the antiferromagnet that is linearly dependent on the applied electric field *E*. The direction of the induced magnetization is determined by the direction of the Néel vector[110]. The induced magnetization gives rise to finite MOKE and MCD signals, whose sign can help determine the AF order. This approach to probing magnetoelectricity in antiferromagnets has recently been demonstrated[104] in bilayer CrI_3, a case we discuss in more detail below. In addition to the $\mathcal{T}\mathcal{I}$ symmetry, a theoretical study has pointed out the importance of the $\mathcal{TM}$ symmetry to the AHE (and therefore to MOKE and MCD) in non-collinear antiferromagnets with kagome lattice structure[109]. In particular, if the $\mathcal{TM}$ symmetry is broken and SOC is present, the off-diagonal conductivity elements $\sigma_{xy} = -\sigma_{yx}$ become non-zero, even the sample magnetization remains zero. The situation may be relevant to the layered frustrated magnets VCl_2 and VBr_2.

Polarization-resolved photoluminescence is another optical technique that has been successfully applied to probe 2D magnetic semiconductors[111]. However, this method is less straightforward to interpret than MOKE or MCD because of complications arising from relaxation processes and potentially extrinsic trapped states. Magnetic linear birefringence and dichroism[96] are also of interest for future studies. In magnetic linear birefringence, one probes the difference in optical refraction for linearly polarized light parallel and perpendicular to the sample magnetization M ($\sigma_{||}^{(2)} - \sigma_{\perp}^{(2)}$), which gives rise to an elliptical polarization. Magnetic linear dichroism is similar, except that one measures the difference in absorption for linearly polarized light parallel and perpendicular to M ($\sigma_{||}^{(1)} - \sigma_{\perp}^{(1)}$), which results in a polarization rotation. In contrast to MOKE and MCD, these ellipticities and rotations are proportional to M^2 and therefore insensitive to the sign of M. These effects are analogous to the anisotropic magnetoresistance (AMR) in electrical transport, rather than the AHE. In the literature, they are often called the Voigt or Cotton–Mouton effects[96]. These techniques should in principle be applicable to either FM or AF materials because of the M^2 dependence[112]. However, application of such techniques to 2D magnetic materials has not yet been demonstrated, likely due to weak signal strengths.

Electrical measurement methods. In addition to optical probes, electrical techniques have also been developed to probe the magnetic state of 2D magnetic materials. The two approaches are related to each other. Whereas optical probes measure the spin-dependent complex optical conductivities[97,98], electrical transport measurements probe the spin-dependent near-DC conductivities[113]. The two types of techniques, however, involve very different experimental approaches. Whereas optical measurements are non-contact in nature, electrical measurements require the fabrication of electrical leads in contact with the materials of interest. The fabrication of an electrical device introduces a variety of measurement and device concepts in addition to the pure characterization of the conductivity of a particular material. Various types of junction geometries can be made, greatly enriching the types of devices relevant to technological applications.

The magnetic state of 2D itinerant magnets with conducting electrons can be probed by AMR and the AHE[114]. Whereas AMR originates from the dependence of the DC conductivity on the magnetization direction (analogous to magnetic linear birefringence/dichroism discussed above), the AHE originates from the antisymmetric off-diagonal elements of the conductivity tensor (analogous to the magnetic circular birefringence/dichroism). The AHE has been applied to study the magnetic order of layered Fe_3GeTe_2 down to the monolayer limit[44]. In contrast to the bulk material, which displays metallic behaviour in electrical transport (decreasing resistivity as a function of decreasing temperature), for monolayer Fe_3GeTe_2 the resistivity increases with decreasing temperature. Nevertheless, the resistance remains measurable down to low temperatures, and AHE has been observed in monolayer Fe_3GeTe_2 below the Curie temperature of ~20 K (FIG. 4a). Very recently, a quantized AHE has been observed in A-type few-layer AF $MnBi_2Te_4$ (REF.[52]).

In addition to in-plane transport measurements, out-of-plane magnetic tunnel junctions in which 2D magnetic materials serve as the electrodes have also been demonstrated[115–117] (FIG. 4b), for example, Fe_3GeTe_2/hBN/Fe_3GeTe_2 structures (hBN is hexagonal boron nitride) and $Fe_{1/4}TaS_2$/oxide/$Cr_{1/3}TaS_2$ structures. A large tunnel magnetoresistance (TMR) of ~160% has been observed on switching between parallel and antiparallel magnetic alignment, demonstrating good efficiency for spin-dependent tunnelling through the van der Waals interfaces.

For the 2D localized-spin systems, most of the materials are highly insulating so that in-plane transport measurements on isolated layers are basically impossible. However, they can still be integrated with other materials to allow the electrical readout of the magnetic orientation. For example, the placement of the 2D magnets on a heavy-metal film can induce a large AHE that indicates whether the magnetic moments at the interface point up or down[118,119].

Insulating 2D magnetic layers can also be used as tunnel barriers to make vertical spin-filter tunnel junction devices[120], providing a fascinating new platform to study spin-dependent tunnelling and to probe the magnetic configuration within the barrier materials. Several research groups independently reported very large values of spin-filter TMR in graphene/CrI_3/graphene tunnel junction devices in 2018 (see REFS[72,86,121,122] and FIG. 4c). As discussed above, 2D CrI_3 is an A-type interlayer AF, which can undergo spin-flip transitions under moderate values of a perpendicular magnetic field to reach FM alignment. Each monolayer of CrI_3 can be thought as a spin filter for electrons, with different tunnel barrier heights for spin-up and spin-down electrons. As spin-unpolarized electrons are injected from the graphene contacts, the electrons see successive anti-aligned spin filters in AF CrI_3. As a result, spin-up and spin-down electrons see approximately the same average tunnel barrier (if there are an even number of CrI_3 layers). For applied fields large enough to align the different CrI_3 layers, the injected electrons see successive aligned spin filters so that the average barrier for one flavour of spins is reduced and the other increased. Due to the exponential dependence of tunnelling probability on barrier height, the result is a much greater overall electron transmission, or a much lower electrical resistance, at large applied magnetic fields. FIGURE 4c shows an example of spin-filter TMR reaching 100% in a graphene/CrI_3/graphene device as the 2D CrI_3 layer undergoes a spin-flip transition from the AF to the FM orientation. Similar values

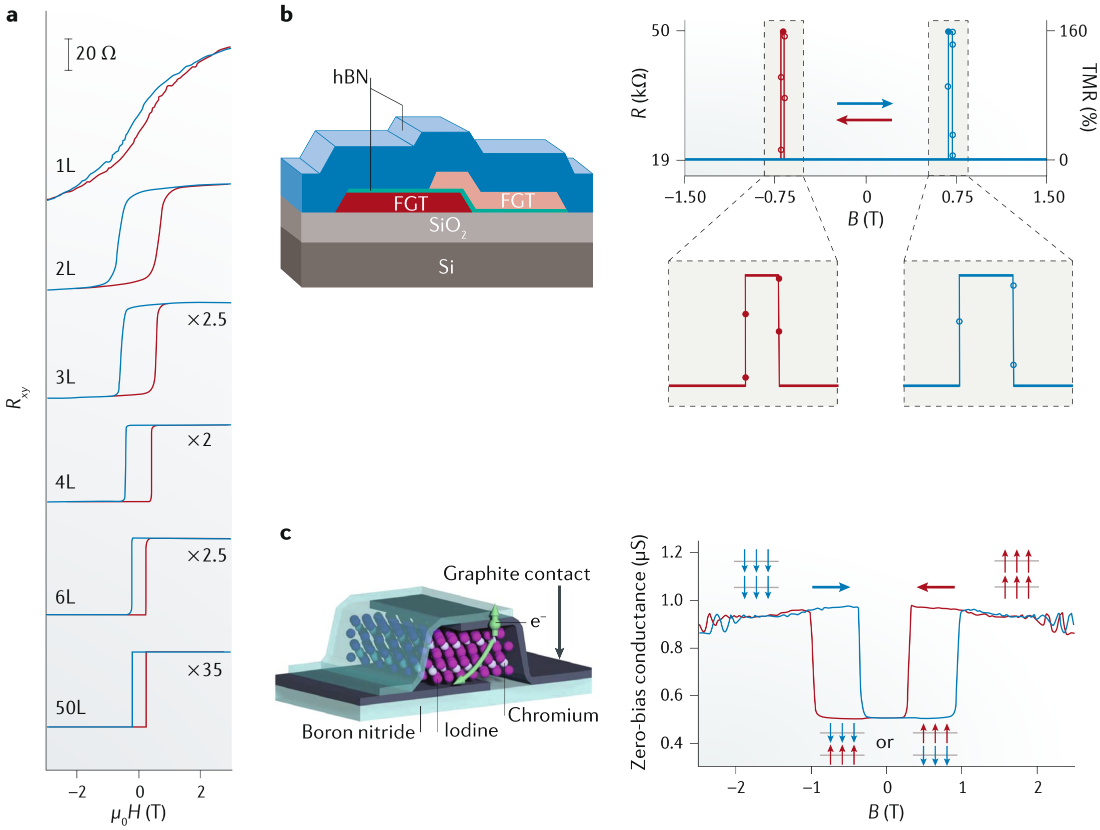

Fig. 4 | **Electrical readout of 2D magnetic states. a** | Probing ferromagnetic (FM) order in 2D Fe_3GeTe_2 by the anomalous Hall effect. Clear FM hysteresis can be seen down to the monolayer limit (1L). **b** | Fe_3GeTe_2/hBN/Fe_3GeTe_2 (hBN, hexagonal boron nitride) tunnel junction exhibits large tunnel magnetoresistance (TMR) when the spins of the two FM layers change from being aligned to anti-aligned. The difference in the coercivity of the two FM layers realizes a spin valve device. **c** | Graphene/bilayer CrI_3/graphene tunnel junction exhibiting large TMR based on spin filtering. The tunnel conductance is small when the bilayer CrI_3 is in the interlayer antiferromagnetic state, and large when the bilayer CrI_3 is in the FM state. In all panels, blue and red correspond to opposing field scanning directions, and the vertical arrows represent the spin orientation. R_{xy}, Hall resistance; μ_0, permeability of free space; *B*, magnetic field; FGT, Fe_3GeTe_2; *H*, external magnetic field; *R*, resistance; R_{xy}, Hall resistance. Panel **a** is adapted from REF.[44], Springer Nature Limited. Panel **b** is adapted with permission from REF.[115], ACS. Panel **c** is adapted with permission from REF.[72], AAAS.

of spin-filter TMR have also been observed for the same kind of devices under in-plane magnetic fields[121,122], which cause a continuous rotation of spins from the out-of-plane alignment in the AF state at zero field to parallel in-plane alignment at high fields. The magnetic anisotropy field of 2D CrI_3 can be determined from such a measurement. The value of spin-filter TMR increases quickly with increasing numbers of CrI_3 layers, with values as large as 10^6% for 10 layers[122]. However, the overall electron transmission decreases exponentially with layer number, giving rise to very large resistances not ideal for technological applications. The current–voltage dependence also becomes highly nonlinear as the CrI_3 thickness increases, which has been ascribed to the onset of electron field emission under high electrical bias. The nonlinear current–voltage characteristics give rise to a bias dependence for the spin-filter TMR, as the onset of field emission is different for the AF and the FM configurations.

The idea of making spin-filter tunnel junctions based on 2D magnetic tunnel barriers should also be applicable to other 2D AF insulators[87,123], such as $FeCl_2$ and $CrCl_3$ (REF.[87]), which like CrI_3 can undergo similar AF–FM switching transitions as a function of applied magnetic field. Carrying out such experiments under a vector magnetic field should yield valuable information about their magnetic exchange and anisotropy energy scales[123]. For 2D FM insulator materials, such as $CrBr_3$ and $CrGeTe_3$, a magnetic field will not drive switching between antiparallel and parallel spin states, and so will not produce large TMR signals. However, tunnelling AMR signals are still expected, originating from a dependence of the effective tunnel barrier height on the direction of the magnetization[124]. Tunnelling AMR is expected to be much weaker compared with spin-filter TMR, and has not yet been demonstrated for tunnel barriers made from 2D ferromagnetic insulators.

Switching 2D magnets by electric fields. The ability to control magnetism by electric field effects in the absence of a charge current is an attractive idea for applications that require fast and energy-efficient magnetic switching[61]. There are several aspects of 2D magnetic materials that are uniquely promising for developing electric field-controlled magnetism. First, the atomic thickness of the material ensures its high sensitivity to electrical perturbations (the material is the surface). Second, the ability to build high-quality van der Waals heterostructures allows the application of very high electric fields (up to ~1 V nm^{-1}) without electrical breakdown[2], crucial for inducing strong effects on the material. Third, the small interlayer exchange energy scale as a result of the weak interlayer bonding means that small external perturbations have the potential to produce significant changes in the magnetic ground state of the material. These aspects together provide strategies that may allow electric field control of magnetism to be much more effective for 2D magnets than in conventional 3D materials. Below, we discuss recent advances in controlling magnetism in 2D magnetic materials by the linear ME effect[104] and by electrostatic doping[103,105].

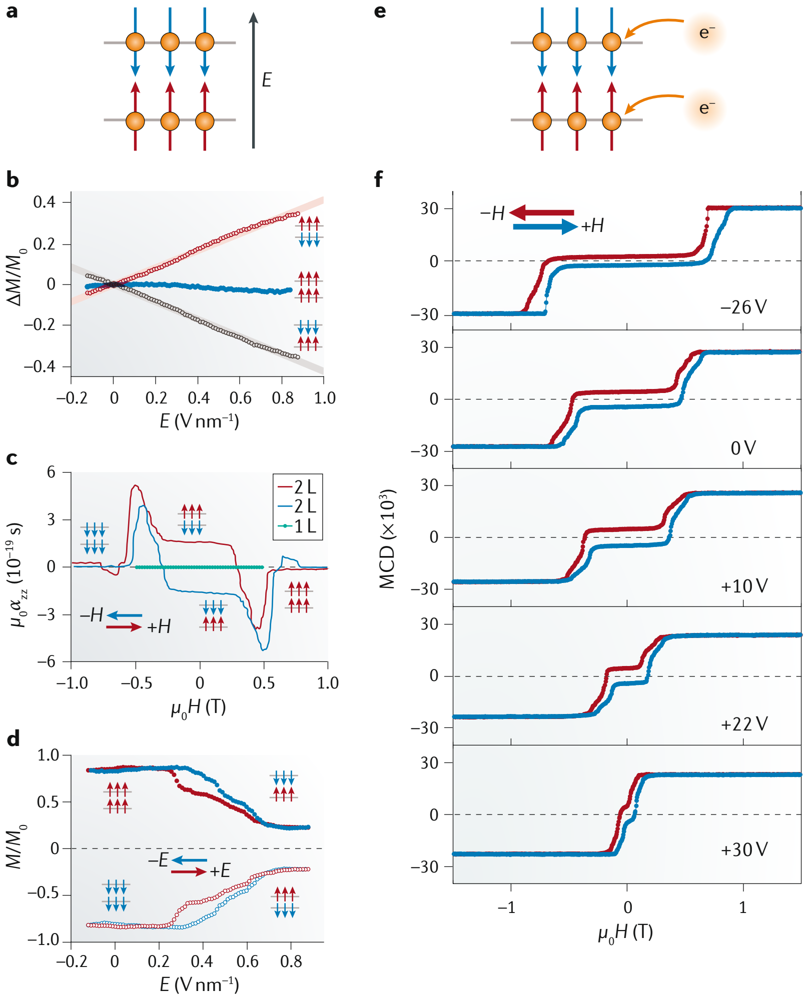

Fig. 5 | **Reorienting and switching 2D magnets by electric fields. a** | Schematic of linear magnetoelectric (ME) effect induced by a vertical electric field E in antiferromagnetic (AF) bilayer CrI_3. **b** | Linear ME effect in AF bilayer CrI_3. The sign of the linear ME effect is determined by the direction of the Néel vector in AF bilayer CrI_3. No linear ME effect is seen in the ferromagnetic (FM) state, which has inversion symmetry. **c** | Magnetic field dependence of the linear ME coefficient in bilayer (2L) CrI_3. A large ME coefficient is seen only in the interlayer AF state with broken inversion symmetry. Negligible ME coefficient is seen in monolayer (1L) and FM bilayer CrI_3. **d** | Electric field dependence of the sample magnetization in bilayer CrI_3 under an external magnetic field of +0.44 T (top) and −0.44 T (bottom), demonstrating reversible electrical switching of the magnetic configuration. **e** | Schematic of introducing electron doping in bilayer CrI_3. **f** | Magnetic field dependence of the magnetic circular dichroism (MCD) signal in bilayer CrI_3 at different gate voltages (which changes doping levels while keeping the interlayer electric field unchanged). For high electron doping densities (positive gate voltages) the material changes almost entirely from an interlayer AF state to a FM state under zero magnetic field. The horizontal arrows in all panels represent the field scanning direction and the vertical arrows represent spin orientation. α_{zz}, the zz component of the ME coefficient of 2L CrI_3; ΔM, change in magnetization; μ_0, permeability of free space; H external magnetic field; M_0, saturation magnetization. Panels **b–d** are adapted from REF.[104], Springer Nature Limited. Panel **f** is adapted from REF.[103], Springer Nature Limited.

The linear ME effect is a linear coupling between magnetization M and an applied electric field E (or between the electrical polarization P and an applied magnetic field H), that is, $M_i = \alpha_{ij}E_j$ (or $P_i = \alpha_{ij}H_j$)[59,60]. Here α_{ij} is an element of the rank-two ME tensor and repeated indices represent summation. The effect originates from a coupling term $\alpha_{ij}E_iH_j$ in the expansion of the free energy of a material under an external electric and magnetic field. Since the inversion $\mathcal{I}$ operation reverses the sign of $E \rightarrow -E$ but not H, whereas time reversal $\mathcal{T}$ reverses the sign of $H \rightarrow -H$ but not E (the free energy must be invariant under both operations), the ME tensor is required to be zero for inversion or time-reversal symmetric materials. The combined operation $\mathcal{TI}$, however, reverses the sign of both E and H so that a ME material can still possess $\mathcal{TI}$ symmetry (only $\mathcal{T}$ and $\mathcal{I}$ are separately broken). The exact form of the ME tensor α_{ij} is determined by the magnetic point group of a ME material[125]. The dimension of α_{ij} in SI unit is seconds per metre. The magnitude of α_{ij} is bounded by the relation $\alpha_{ij} < \sqrt{\varepsilon_i \mu_j}$ (one over the speed of light in the material)[59]. Here ε_i and μ_j are elements of the electric permittivity and magnetic permeability tensor of the ME material, respectively. Therefore, magnetic and electric ordered materials with large ε_i and μ_j typically show stronger ME effects. Microscopic contributions to α_{ij} can include electronic and lattice effects, as well as spin and orbital contributions[126].

Bilayer CrI_3 is the first 2D magnetic material in which a linear ME coupling has been demonstrated[104]. For magnetic fields smaller than the spin-flip transition field, the material is an A-type interlayer AF (FIG. 1b), which breaks time-reversal symmetry. The total structure including the spins also breaks inversion symmetry (that is, the magnetic point group does not have an inversion centre). The combined $\mathcal{TI}$ operation, however, remains a good symmetry. As a result, a linear ME effect is expected. Indeed, by measuring the sample magnetization through MCD under varying vertical electric fields E_z while keeping the doping level in the material constant, an induced magnetization $M_z = \alpha_{zz}E_z$, linearly proportional to E_z, has been observed in the AF state (FIG. 5b). Furthermore, by reversing the AF-Néel vector through ME annealing, the sign of the ME coefficient α_{zz} is reversed, demonstrating the ability to distinguish different AF states in 2D materials with this technique. When the material is saturated to an FM configuration under an external magnetic field, the ME effect vanishes as expected from the restoration of inversion symmetry in the FM state. The saturation magnetization is therefore not modified by the ME effect. The dependence of the ME coefficient α_{zz} on external magnetic field is summarized in FIG. 5c.

A large α_{zz} is observed near the spin-flip transition field, because at this point small changes in interactions can generate large changes in spin orientation. This makes the value of the magnetic field required for the spin flip dependent on the electric field. By biasing the material with a constant magnetic field near the spin-flip field, complete and reversible switching of the material between the AF and the FM state by pure electric fields can be achieved (FIG. 5d).

In addition to electric fields, electrostatic doping (without changing the interlayer electric field) can also be used to control magnetism in 2D CrI_3 (REFS[103,105]) and $CrGeTe_3$ (REF.[127]) (FIG. 5e). Electrostatically doping a magnetic material is expected to modify the occupancy of the magnetic ion and the exchange coupling strength, the latter being extremely sensitive to the amount of wavefunction overlap between atomic orbitals. Indeed, in contrast to the ME effect, varying the doping level in monolayer CrI_3 in a field-effect device modifies the saturation magnetization. The transition temperature T_C can also be modulated[103] by 10 K (from 50 K to 40 K), which corresponds to a change in the intralayer exchange integral $\Delta J_{||} \sim 0.4$ meV. Meanwhile, a simple estimate from the measured spin-flip transition field $H_C \sim 0.5$ T in bilayer CrI_3 yields an interlayer exchange integral $J_\perp \sim 2\mu_B H_C \sim 0.1$ meV. The significant doping modulation in $J_{||}$ therefore suggests that electrostatic doping could effectively modulate and switch the interlayer magnetic order in 2D CrI_3. The magnetic field dependence of the sample magnetization of bilayer CrI_3 at varying doping levels is shown in FIG. 5f. A change in the ground state from the AF to FM alignment is observed at high doping densities with a fixed value of applied magnetic field near the spin-flip transition. Such effective doping control of the spin-flip transition field can allow complete and reversible electrical switching of bilayer CrI_3 between the AF and the FM states at greatly reduced external magnetic biases. Further improvement in introducing electron doping in the material could allow electrical switching of magnetism under zero magnetic bias, the ideal goal for device applications[61].

Emerging device concepts. The unique properties of 2D magnetic materials have already inspired new device concepts and are likely to inspire many more. Here we briefly discuss two examples: one makes use of electrically switchable magnetization to realize a new type of spin transistors[128], and the other uses the atomically flat surfaces of 2D magnets to induce magnetic proximity coupling to monolayer semiconductors[24]. There is also a theoretical proposal for spin-valve devices based on graphene/CrI_3 heterostructures[129], which have not yet been realized.

By fabricating a dual-gated tunnel junction of bilayer (2L) graphene/2L CrI_3/2L graphene (FIG. 6a), it was recently found that a tunnel field-effect transistor (TFET) with a large on–off ratio can be realized[103,128]. The large on–off ratio is caused by the opening of a bandgap in asymmetric 2L graphene, which forbids quantum tunnelling when the Fermi level is tuned by the gates into the bandgap. In addition, because the tunnel barrier (bilayer CrI_3) is magnetic, the transistor output is spin dependent. Strongly enhanced TMR and even negative TMR have been observed near the TFET on–off threshold. Furthermore, by combining the spin filtering effect and the electrically switchable AF–FM transition in bilayer CrI_3 as discussed above, a spin TFET can be realized under a constant magnetic bias, in which the device's high and low resistance states can be controlled by electrically switching the few-layer CrI_3 tunnel barrier between the AF and the FM configurations (FIG. 6b). An on–off ratio over 400% has been realized. This device concept may find interesting applications for voltage-controlled magnetic random access memory devices.

Another interesting device concept is realized by coupling monolayer WSe_2 (a direct bandgap semiconductor) to 2D CrI_3 (REF.[24]). Although 2D CrI_3 is an antiferromagnet, its surface is fully uncompensated (all surface spins are aligned parallel) and free of dangling bonds. As a result, a strong magnetic proximity coupling between the two materials is expected. Indeed, below the Curie temperature of CrI_3, spontaneous circularly polarized photoluminescence (PL) from monolayer WSe_2 has been observed under zero magnetic field and linearly polarized optical pumping (FIG. 6c,d). A spontaneous Zeeman splitting ~2 meV between left-handed and right-handed PL has also been seen. Furthermore, through magnetic field-dependence studies, both the PL handedness and the Zeeman splitting have been shown to depend on the magnetization of the underlying CrI_3 layer. The results are fully consistent with the picture of lifted valley degeneracy in monolayer WSe_2 when it is proximity coupled to the magnetic surface of 2D CrI_3 (FIG. 6c). The magnetic proximity exchange interaction at the interface polarizes the valley magnetic moments of WSe_2, and produces the spontaneous PL handedness and valley Zeeman splitting. When this is combined with the electrically switchable magnetic order in CrI_3, one could envision pure electrical control of valley polarization in monolayer semiconductors, which may find interesting applications in spin-dependent optoelectronics and photonics.

Challenges and opportunities

The study of 2D magnetic materials is just beginning. No one can predict what new discoveries might emerge. However, we close by pointing out some of the remaining challenges that must be overcome to enable useful applications, and some emerging scientific opportunities that seem particularly promising.

Two-dimensional magnetic materials offer potential for dramatic improvements in spintronic devices for memory and logic, but this will require the understanding of how to both write and read their magnetic states in the best way. It will be valuable to explore many different strategies that might be used to manipulate magnetic states for writing — both mechanisms that have been previously demonstrated using 3D magnetic materials[17] (for example, spin-transfer torque, spin–orbit torque, voltage-controlled magnetic anisotropy and optical techniques) and new mechanisms enabled by the structure of 2D materials[103–105,127] (for example, ME effects, doping and strain). Ultimately, different mechanisms might be

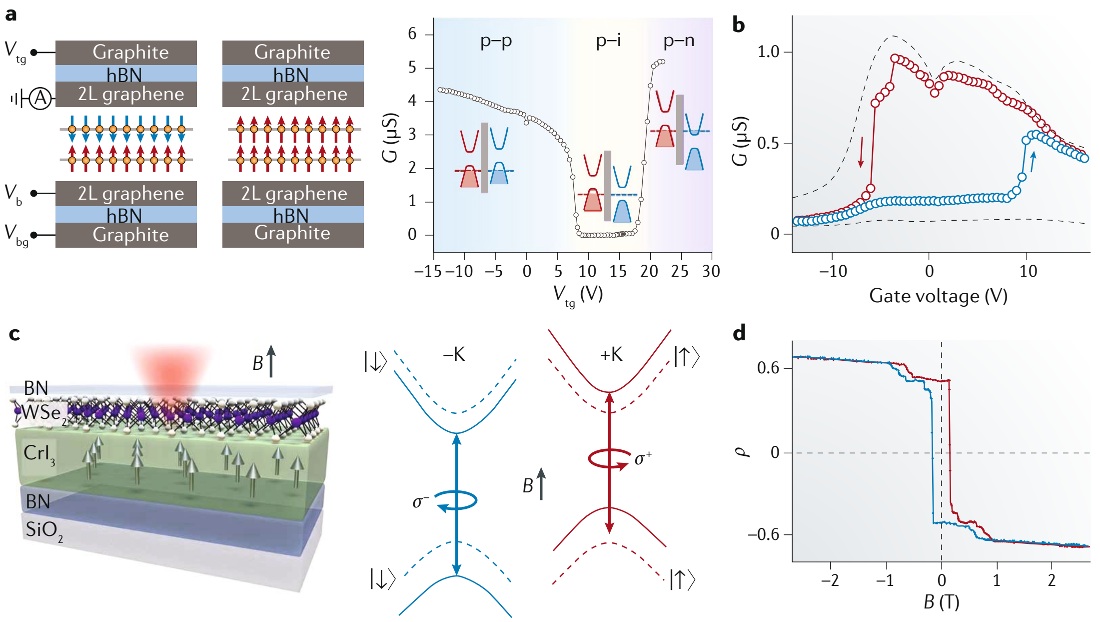

Fig. 6 | **Spin transistors and the van der Waals magnetic proximity effect. a** | Spin tunnel field-effect transistors based on dual-gated graphene/CrI$_3$/graphene tunnel junction. The two transistors are in a low tunnel conductance state (left schematic) and a high tunnel conductance state (right schematic). The top gate voltage (V_{tg}) dependence of the tunnel conductance G demonstrates the operation of the device (right plot). The band alignments corresponding to different conductance states are shown. Blue, white and purple denote p–p, p–i and p–n junctions, respectively. Here p is hole-doped, i is intrinsic and n is electron-doped graphene. **b** | Gate-voltage dependence of G under an external magnetic field of 1.77 T. The hysteresis loop originates from electrical switching of the magnetic configuration of the CrI$_3$ barrier. The dashed lines show the conductance states under 0 T (low-conductance antiferromagnetic state) and 2 T (high-conductance ferromagnetic state). Red and blue correspond to opposing field scanning directions. **c** | Magnetic proximity coupling between monolayer WSe$_2$ and 2D CrI$_3$ (left) induces valley splitting in the WSe$_2$ layer (right). The dashed and solid lines represent the band structure of monolayer WSe$_2$ without and with magnetic proximity coupling. ↑ and ↓ denote the spin orientations. +K and –K denote the two different Brillouin zone corners. σ^+ and σ^- denote left-handed and right-handed optical transitions. **d** | Magnetic field dependence of the photoluminescence handedness ρ from monolayer WSe$_2$ coupled to 2D CrI$_3$. Error bars are smaller than the symbols. The hysteresis loop demonstrates the spontaneous valley polarization under zero magnetic field due to magnetic proximity coupling of the WSe$_2$ layer to the adjacent ferromagnetic CrI$_3$ layer. Red and blue correspond to opposing field scanning directions. 2L graphene, bilayer graphene; B, magnetic field; hBN, hexagonal boron nitride; V_b, bias voltage; V_{bg}, bottom gate voltage. Panels **a,b** are adapted from REF.[128], Springer Nature Limited. Panels **c,d** are adapted with permission from REF.[24], AAAS.

used in combination for the best results. The explorations of how applied electric fields and strain may affect the full spectrum of magnetic properties (such as interlayer exchange interactions, magnetic damping, magnetic anisotropy, Dzyaloshinskii–Moriya interactions) are almost certain to uncover interesting new physics, and will likely require the development of new experimental techniques to deal with small sample volumes. Studies regarding the generation and propagation of spin waves in 2D magnets[76] will also be of both fundamental and potential practical interest.

For readout of magnetic states, the demonstration of very large TMR effects in spin-filter tunnel junctions incorporating 2D magnetic tunnel barriers[72,86,121,122] is certainly exciting — we have noted that even these first spin-filter devices demonstrated larger TMR ratios than state-of-the-art conventional tunnel junctions[130], albeit at cryogenic temperatures. However, it is important to point out that the resistances demonstrated so far in graphite/multilayer CrI$_3$/graphite spin-filter tunnel junctions are probably much too high to be practical. If these devices are scaled below 100 nm dimensions, the on-state resistance will be >1 GΩ even for the lowest-resistance bilayer CrI$_3$ devices, whereas for incorporation with practical CMOS circuitry the resistance should not be greater than tens of kΩ. One could say that the existing devices have large 'off–off ratios' rather than large on–off ratios. It will be interesting to see the extent to which the resistances can be decreased using electrode metals with electronic densities of states larger than in graphite, or whether other readout strategies based on interlayer exchange interactions or magnetic proximity effects might prove superior. It will also be important to develop device structures that are bistable and switchable at zero applied magnetic field, rather than hysteretic only at non-zero field values.

For the majority of imaginable spintronics applications, but not all, the 2D materials must have magnetic states that are stable at room temperature. They will need to be produced at the full-wafer scale and integrated into 3D heterostructures while maintaining clean, high-quality interfaces. These will be major challenges, particularly since many of the materials are unstable on exposure to air.

Looking beyond simple ferromagnets, we expect that 2D magnetic materials have the potential to enable wide-ranging new studies on many kinds of magnetic states — including antiferromagnets, spin liquids and spatially non-uniform spin textures such as magnetic skyrmions[30–32]. We are particularly excited about experiments on 2D antiferromagnets. For instance, the type-A antiferromagnets with parallel spins within each layer and antiparallel configurations in adjacent layers provide for the first time the possibility to directly address different spin sublattices within an antiferromagnet independently, for example, using separate spin–orbit torques applied to the top and bottom of a sample with an even number of magnetic layers. This should provide new insights about the fundamental dynamics within antiferromagnets, and perhaps a route towards making spin-torque nano-oscillators based on antiferromagnetic spin resonances with frequencies far above the gigahertz range of nano-oscillators made with ferromagnets[74,131]. Progress in studying antiferromagnets and other states consisting of spatially non-uniform spins will likely be accelerated by new high-resolution probes of magnetic states. Recent advances in scanning tunnelling microscopy and scanning transmission electron microscopy[132] suggest promising routes to achieve magnetic imaging with sensitivity near the atomic scale.

We furthermore foresee that 2D magnets can be an important resource for the design and development of new quantum materials made by assembling 2D van der Waals layers into 3D heterostructures[2]. These heterostructures can provide the precision control over the breaking of time-reversal and inversion symmetries that is needed to construct new topological materials. For example, the coupling between 2D magnets and 2D superconductors[133] is a promising route for the demonstration of topological superconductors[134], and the breaking of time-reversal symmetry is one route for the creation of Weyl semimetals[135]. Coupling to other types of electronic matter — ferroelectrics, multiferroics, materials with strong spin–orbit interactions, valley ferromagnets and so on — should give rise to other collective states with interesting and potentially useful properties.

1. Geim, A. K. & Novoselov, K. S. The rise of graphene. *Nat. Mater.* **6**, 183–191 (2007).
2. Geim, A. K. & Grigorieva, I. V. Van der Waals heterostructures. *Nature* **499**, 419–425 (2013).
3. Manzeli, S., Ovchinnikov, D., Pasquier, D., Yazyev, O. V. & Kis, A. 2D transition metal dichalcogenides. *Nat. Rev. Mater.* **2**, 17033 (2017).
4. Han, W., Kawakami, R. K., Gmitra, M. & Fabian, J. Graphene spintronics. *Nat. Nanotechnol.* **9**, 794 (2014).
5. Tongay, S., Varnoosfaderani, S. S., Appleton, B. R., Wu, J. & Hebard, A. F. Magnetic properties of MoS$_2$: existence of ferromagnetism. *Appl. Phys. Lett.* **101**, 123105 (2012).
6. Yan, S. et al. Enhancement of magnetism by structural phase transition in MoS$_2$. *Appl. Phys. Lett.* **106**, 012408 (2015).
7. Guguchia, Z. et al. Magnetism in semiconducting molybdenum dichalcogenides. *Sci. Adv.* **4**, eaat3672 (2018).
8. Chittari, B. L. et al. Electronic and magnetic properties of single-layer MPX$_3$ metal phosphorous trichalcogenides. *Phys. Rev. B* **94**, 184428 (2016).
9. Liu, J., Sun, Q., Kawazoe, Y. & Jena, P. Exfoliating biocompatible ferromagnetic Cr-trihalide monolayers. *Phys. Chem. Chem. Phys.* **18**, 8777–8784 (2016).
10. Sivadas, N., Daniels, M. W., Swendsen, R. H., Okamoto, S. & Xiao, D. Magnetic ground state of semiconducting transition-metal trichalcogenide monolayers. *Phys. Rev. B* **91**, 235425 (2015).
11. Wang, H., Eyert, V. & Schwingenschlögl, U. Electronic structure and magnetic ordering of the semiconducting chromium trihalides CrCl$_3$, CrBr$_3$, and CrI$_3$. *J. Phys. Condens. Matter* **23**, 116003 (2011).
12. Zhang, W.-B., Qu, Q., Zhu, P. & Lam, C.-H. Robust intrinsic ferromagnetism and half semiconductivity in stable two-dimensional single-layer chromium trihalides. *J. Mater. Chem. C.* **3**, 12457–12468 (2015).
13. Lebègue, S., Björkman, T., Klintenberg, M., Nieminen, R. M. & Eriksson, O. Two-dimensional materials from data filtering and ab initio calculations. *Phys. Rev. X* **3**, 031002 (2013).
14. Li, X., Cao, T., Niu, Q., Shi, J. & Feng, J. Coupling the valley degree of freedom to antiferromagnetic order. *Proc. Natl Acad. Sci. USA* **110**, 3738–3742 (2013).
15. Gong, C. et al. Discovery of intrinsic ferromagnetism in two-dimensional van der Waals crystals. *Nature* **546**, 265–269 (2017).
The first optical probe of magnetic states in 2D Cr$_2$Ge$_2$Te$_6$.
16. Huang, B. et al. Layer-dependent ferromagnetism in a van der Waals crystal down to the monolayer limit. *Nature* **546**, 270–273 (2017).
The first demonstration of layer number dependent magnetic states in 2D CrI$_3$.
17. Hellman, F. et al. Interface-induced phenomena in magnetism. *Rev. Mod. Phys.* **89**, 025006 (2017).
18. Sander, D. et al. The 2017 magnetism roadmap. *J. Phys. D* **50**, 363001 (2017).
19. Bromberg, D. M., Morris, D. H., Pileggi, L. & Zhu, J. Novel STT-MTJ device enabling all-metallic logic circuits. *IEEE Trans. Magn.* **48**, 3215–3218 (2012).
20. Datta, S., Salahuddin, S. & Behin-Aein, B. Non-volatile spin switch for Boolean and non-Boolean logic. *Appl. Phys. Lett.* **101**, 252411 (2012).
21. Arias, R. & Mills, D. L. Extrinsic contributions to the ferromagnetic resonance response of ultrathin films. *Phys. Rev. B* **60**, 7395–7409 (1999).
22. Kang, K. et al. Layer-by-layer assembly of two-dimensional materials into wafer-scale heterostructures. *Nature* **550**, 229–233 (2017).
23. Fisher, M. E. The renormalization group in the theory of critical behavior. *Rev. Mod. Phys.* **46**, 597–616 (1974).
24. Zhong, D. et al. Van der Waals engineering of ferromagnetic semiconductor heterostructures for spin and valleytronics. *Sci. Adv.* **3**, e1603113 (2017).
25. Mak, K. F., Xiao, D. & Shan, J. Light–valley interactions in 2D semiconductors. *Nat. Photon.* **12**, 451–460 (2018).
26. Xu, X., Yao, W., Xiao, D. & Heinz, T. F. Spin and pseudospins in layered transition metal dichalcogenides. *Nat. Phys.* **10**, 343–350 (2014).
27. Eschrig, M. Spin-polarized supercurrents for spintronics. *Phys. Today* **64**, 43–49 (2010).
28. Hasan, M. Z. & Kane, C. L. Colloquium: topological insulators. *Rev. Mod. Phys.* **82**, 3045–3067 (2010).
29. Sivadas, N., Okamoto, S., Xu, X., Fennie, C. J. & Xiao, D. Stacking-dependent magnetism in bilayer CrI$_3$. *Nano Lett.* **18**, 7658–7664 (2018).
30. Tong, Q., Liu, F., Xiao, J. & Yao, W. Skyrmions in the moiré of van der Waals 2D magnets. *Nano Lett.* **18**, 7194–7199 (2018).
31. McGuire, M. A. Crystal and magnetic structures in layered, transition metal dihalides and trihalides. *Crystals* **7**, 121 (2017).
32. Brec, R. Review on structural and chemical properties of transition metal phosphorous trisulfides MPS$_3$. *Solid State Ion.* **22**, 3–30 (1986).
33. Susner, M. A., Chyasnavichyus, M., McGuire, M. A., Ganesh, P. & Maksymovych, P. Metal thio- and selenophosphates as multifunctional van der waals layered materials. *Adv. Mater.* **29**, 1602852 (2017).
34. Burch, K. S., Mandrus, D. & Park, J.-G. Magnetism in two-dimensional van der Waals materials. *Nature* **563**, 47–52 (2018).
35. Gong, C. & Zhang, X. Two-dimensional magnetic crystals and emergent heterostructure devices. *Science* **363**, eaav4450 (2019).
36. Gibertini, M., Koperski, M., Morpurgo, A. F. & Novoselov, K. S. Magnetic 2D materials and heterostructures. *Nat. Nanotechnol.* **14**, 408–419 (2019).
37. McGuire, M. A., Dixit, H., Cooper, V. R. & Sales, B. C. Coupling of crystal structure and magnetism in the layered, ferromagnetic insulator CrI$_3$. *Chem. Mater.* **27**, 612–620 (2015).
38. Khomskii, D. I. in *Transition Metal Compounds* Ch. 2 (Cambridge Univ. Press, 2014).
39. Stamokostas, G. L. & Fiete, G. A. Mixing of t_{2g}–e_g orbitals in 4*d* and 5*d* transition metal oxides. *Phys. Rev. B* **97**, 085150 (2018).
40. Feldkemper, S. & Weber, W. Generalized calculation of magnetic coupling constants for Mott–Hubbard insulators: application to ferromagnetic Cr compounds. *Phys. Rev. B* **57**, 7755–7766 (1998).
41. Lado, J. L. & Fernández-Rossier, J. On the origin of magnetic anisotropy in two dimensional CrI$_3$. *2D Mater.* **4**, 035002 (2017).
42. Chang, C.-Z. et al. Experimental observation of the quantum anomalous Hall effect in a magnetic topological insulator. *Science* **340**, 167–170 (2013).
43. Siberchicot, B., Jobic, S., Carteaux, V., Gressier, P. & Ouvrard, G. Band structure calculations of ferromagnetic chromium tellurides CrSiTe$_3$ and CrGeTe$_3$. *J. Phys. Chem.* **100**, 5863–5867 (1996).
44. Deng, Y. et al. Gate-tunable room-temperature ferromagnetism in two-dimensional Fe$_3$GeTe$_2$. *Nature* **563**, 94–99 (2018).
45. Fei, Z. et al. Two-dimensional itinerant ferromagnetism in atomically thin Fe$_3$GeTe$_2$. *Nat. Mater.* **17**, 778–782 (2018).
46. Morosan, E. et al. Sharp switching of the magnetization in Fe$_{1/4}$TaS$_2$. *Phys. Rev. B* **75**, 104401 (2007).
47. Baltz, V. et al. Antiferromagnetic spintronics. *Rev. Mod. Phys.* **90**, 015005 (2018).
48. Ressouche, E. et al. Magnetoelectric MnPS$_3$ as a candidate for ferrotoroidicity. *Phys. Rev. B* **82**, 100408 (2010).
49. Kuhlow, B. Magnetic ordering in CrCl$_3$ at the phase transition. *Phys. Status Solidi A* **72**, 161–168 (1982).
50. Jacobs, I. S. & Lawrence, P. E. Metamagnetic phase transitions and hysteresis in FeCl$_2$. *Phys. Rev.* **164**, 866–878 (1967).
51. Wilkinson, M. K., Cable, J. W., Wollan, E. O. & Koehler, W. C. Neutron diffraction investigations of the magnetic ordering in FeBr$_2$, CoBr$_2$, FeCl$_2$, and CoCl$_2$. *Phys. Rev.* **113**, 497–507 (1959).

52. Deng, Y. et al. Magnetic-field-induced quantized anomalous Hall effect in intrinsic magnetic topological insulator $MnBi_2Te_4$. Preprint at https://arxiv.org/abs/1904.11468 (2019).
53. Tsubokawa, I. On the magnetic properties of a $CrBr_3$ single crystal. *J. Phys. Soc. Jpn* **15**, 1664–1668 (1960).
54. Rule, K. C., McIntyre, G. J., Kennedy, S. J. & Hicks, T. J. Single-crystal and powder neutron diffraction experiments on $FePS_3$: search for the magnetic structure. *Phys. Rev. B* **76**, 134402 (2007).
55. Wildes, A. R. et al. Magnetic structure of the quasi-two-dimensional antiferromagnet $NiPS_3$. *Phys. Rev. B* **92**, 224408 (2015).
56. Tokunaga, Y. et al. Multiferroicity in $NiBr_2$ with long-wavelength cycloidal spin structure on a triangular lattice. *Phys. Rev. B* **84**, 060406 (2011).
57. Kurumaji, T. et al. Magnetoelectric responses induced by domain rearrangement and spin structural change in triangular-lattice helimagnets NiI_2 and CoI_2. *Phys. Rev. B* **87**, 014429 (2013).
58. Kurumaji, T. et al. Magnetic-field induced competition of two multiferroic orders in a triangular-lattice helimagnet MnI_2. *Phys. Rev. Lett.* **106**, 167206 (2011).
59. Manfred, F. Revival of the magnetoelectric effect. *J. Phys. D* **38**, R123 (2005).
60. Rivera, J.-P. A short review of the magnetoelectric effect and related experimental techniques on single phase (multi-) ferroics. *Eur. Phys. J. B* **71**, 299–313 (2009).
61. Matsukura, F., Tokura, Y. & Ohno, H. Control of magnetism by electric fields. *Nat. Nanotechnol.* **10**, 209–220 (2015).
62. Essin, A. M., Moore, J. E. & Vanderbilt, D. Magnetoelectric polarizability and axion electrodynamics in crystalline insulators. *Phys. Rev. Lett.* **102**, 146805 (2009).
63. Hirakawa, K., Kadowaki, H. & Ubukoshi, K. Study of frustration effects in two-dimensional triangular lattice antiferromagnets–neutron powder diffraction study of VX_2, X≡Cl, Br and I. *J. Phys. Soc. Jpn* **52**, 1814–1824 (1983).
64. Johnson, R. D. et al. Monoclinic crystal structure of α–$RuCl_3$ and the zigzag antiferromagnetic ground state. *Phys. Rev. B* **92**, 235119 (2015).
65. Kim, H.-S., V, V. S., Catuneanu, A. & Kee, H.-Y. Kitaev magnetism in honeycomb $RuCl_3$ with intermediate spin-orbit coupling. *Phys. Rev. B* **91**, 241110 (2015).
66. Plumb, K. W. et al. α–$RuCl_3$: a spin-orbit assisted Mott insulator on a honeycomb lattice. *Phys. Rev. B* **90**, 041112 (2014).
67. Banerjee, A. et al. Proximate Kitaev quantum spin liquid behaviour in a honeycomb magnet. *Nat. Mater.* **15**, 733–740 (2016).
68. Kasahara, Y. et al. Majorana quantization and half-integer thermal quantum Hall effect in a Kitaev spin liquid. *Nature* **559**, 227–231 (2018).
69. Sivadas, N., Okamoto, S. & Xiao, D. Gate-controllable magneto-optic Kerr effect in layered collinear antiferromagnets. *Phys. Rev. Lett.* **117**, 267203 (2016).
70. Jiang, P. et al. Stacking tunable interlayer magnetism in bilayer CrI_3. *Phys. Rev. B* **99**, 144401 (2019).
71. Cheng, R., Okamoto, S. & Xiao, D. Spin Nernst effect of magnons in collinear antiferromagnets. *Phys. Rev. Lett.* **117**, 217202 (2016).
72. Klein, D. R. et al. Probing magnetism in 2D van der Waals crystalline insulators via electron tunneling. *Science* **360**, 1218–1222 (2018).
    The first demonstration of spin filtering and giant tunnel magnetoresistance using 2D CrI_3 as a tunnel barrier.
73. Zhang, X. et al. Magnetic anisotropy of the single-crystalline ferromagnetic insulator $Cr_2Ge_2Te_6$. *Jpn J. Appl. Phys.* **55**, 033001 (2016).
74. MacNeill, D. et al. Gigahertz frequency antiferromagnetic resonance and strong magnon–magnon coupling in the layered crystal $CrCl_3$. *Phys. Rev. Lett.* **123**, 047204 (2019).
75. Ghazaryan, D. et al. Magnon-assisted tunnelling in van der Waals heterostructures based on $CrBr_3$. *Nat. Electron.* **1**, 344–349 (2018).
76. Xing, W. et al. Magnon transport in quasi-two-dimensional van der waals antiferromagnets. *Phys. Rev. X* **9**, 011026 (2019).
77. Pershoguba, S. S. et al. Dirac magnons in honeycomb ferromagnets. *Phys. Rev. X* **8**, 011010 (2018).
78. Chen, L. et al. Topological spin excitations in honeycomb ferromagnet CrI_3. *Phys. Rev. X* **8**, 041028 (2018).
79. Lee, J.-U. et al. Ising-type magnetic ordering in atomically thin $FePS_3$. *Nano Lett.* **16**, 7433–7438 (2016).
80. Du, K.-z et al. Weak van der waals stacking, wide-range band gap, and raman study on ultrathin layers of metal phosphorus trichalcogenides. *ACS Nano* **10**, 1738–1743 (2016).
81. Zhou, B. et al. Possible structural transformation and enhanced magnetic fluctuations in exfoliated α-$RuCl_3$. *J. Phys. Chem. Solids* **128**, 291–295 (2018).
82. Lin, M.-W. et al. Ultrathin nanosheets of $CrSiTe_3$: a semiconducting two-dimensional ferromagnetic material. *J. Mater. Chem. C* **4**, 315–322 (2016).
83. Tian, Y., Gray, M. J., Ji, H., Cava, R. J. & Burch, K. S. Magneto-elastic coupling in a potential ferromagnetic 2D atomic crystal. *2D Mater.* **3**, 025035 (2016).
84. Jin, W. et al. Raman fingerprint of two terahertz spin wave branches in a two-dimensional honeycomb Ising ferromagnet. *Nat. Commun.* **9**, 5122 (2018).
85. Soriano, D., Cardoso, C. & Fernández-Rossier, J. Interplay between interlayer exchange and stacking in CrI_3 bilayers. *Solid State Commun.* **299**, 113662 (2019).
86. Wang, Z. et al. Very large tunneling magnetoresistance in layered magnetic semiconductor CrI_3. *Nat. Commun.* **9**, 2516 (2018).
    The first demonstration of spin filtering and giant tunnel magnetoresistance using 2D CrI_3 as a tunnel barrier.
87. Klein, D. R. et al. Giant enhancement of interlayer exchange in an ultrathin 2D magnet. Preprint at https://arxiv.org/abs/1903.00002 (2019).
88. Sun, Z. et al. Giant and nonreciprocal second harmonic generation from layered antiferromagnetism in bilayer CrI_3. *Nature* **572**, 497–501 (2019).
89. Li, T. et al. Pressure-controlled interlayer magnetism in atomically thin CrI_3. Preprint at https://arxiv.org/abs/1905.10905 (2019).
90. Song, T. et al. Switching 2D magnetic states via pressure tuning of layer stacking. Preprint at https://arxiv.org/abs/1905.10860 (2019).
91. Mermin, N. D. & Wagner, H. Absence of ferromagnetism or antiferromagnetism in one- or two-dimensional isotropic Heisenberg models. *Phys. Rev. Lett.* **17**, 1133–1136 (1966).
92. Bonilla, M. et al. Strong room-temperature ferromagnetism in VSe_2 monolayers on van der Waals substrates. *Nat. Nanotechnol.* **13**, 289–293 (2018).
93. Ma, Y. et al. Evidence of the existence of magnetism in pristine VX_2 monolayers (X = S, Se) and their strain-induced tunable magnetic properties. *ACS Nano* **6**, 1695–1701 (2012).
94. Fuh, H.-R., Yan, B., Wu, S.-C., Felser, C. & Chang, C.-R. Metal-insulator transition and the anomalous Hall effect in the layered magnetic materials VS_2 and VSe_2. *New J. Phys.* **18**, 113038 (2016).
95. O'Hara, D. J. et al. Room temperature intrinsic ferromagnetism in epitaxial manganese selenide films in the monolayer limit. *Nano Lett.* **18**, 3125–3131 (2018).
96. Weiglhofer, W. S. & Lakhtakia, A. (eds) *Introduction to Complex Mediums for Optics and Electromagnetics* 175 (SPIE, 2003).
97. Schubert, M., Kühne, P., Darakchieva, V. & Hofmann, T. Optical Hall effect — model description: tutorial. *J. Opt. Soc. Am. A* **33**, 1553–1568 (2016).
98. Argyres, P. N. Theory of the Faraday and Kerr effects in ferromagnetics. *Phys. Rev.* **97**, 334–345 (1955).
99. Thiel, L. et al. Probing magnetism in 2D materials at the nanoscale with single-spin microscopy. *Science* **364**, 973–976 (2019).
100. Kapitulnik, A., Xia, J., Schemm, E. & Palevski, A. Polar Kerr effect as probe for time-reversal symmetry breaking in unconventional superconductors. *New J. Phys.* **11**, 055060 (2009).
101. Sato, K. Measurement of magneto-optical Kerr effect using piezo-birefringent modulator. *Jpn J. Appl. Phys.* **20**, 2403–2409 (1981).
102. Lee, J.-W., Kim, J., Kim, S.-K., Jeong, J.-R. & Shin, S.-C. Full vectorial spin-reorientation transition and magnetization reversal study in ultrathin ferromagnetic films using magneto-optical Kerr effects. *Phys. Rev. B* **65**, 144437 (2002).
103. Jiang, S., Li, L., Wang, Z., Mak, K. F. & Shan, J. Controlling magnetism in 2D CrI_3 by electrostatic doping. *Nat. Nanotechnol.* **13**, 549–553 (2018).
    Demonstration of efficient tuning of magnetic states in bilayer CrI_3 by electrostatic doping.
104. Jiang, S., Shan, J. & Mak, K. F. Electric-field switching of two-dimensional van der Waals magnets. *Nat. Mater.* **17**, 406–410 (2018).
    The first demonstration of magnetoelectricity in antiferromagnetic bilayer CrI_3.
105. Huang, B. et al. Electrical control of 2D magnetism in bilayer CrI_3. *Nat. Nanotechnol.* **13**, 544–548 (2018).
    Demonstration of tuning of magnetic states in bilayer CrI_3 by electric field effects.
106. Lee, J., Mak, K. F. & Shan, J. Electrical control of the valley Hall effect in bilayer MoS_2 transistors. *Nat. Nanotechnol.* **11**, 421–425 (2016).
107. Lee, J., Wang, Z., Xie, H., Mak, K. F. & Shan, J. Valley magnetoelectricity in single-layer MoS_2. *Nat. Mater.* **16**, 887–891 (2017).
108. O'Dell, T. H. The electrodynamics of magneto-electric media. *Phil. Mag.* **7**, 1653–1669 (1962).
109. Chen, H., Niu, Q. & MacDonald, A. H. Anomalous Hall effect arising from noncollinear antiferromagnetism. *Phys. Rev. Lett.* **112**, 017205 (2014).
110. Rado, G. T. Magnetoelectric evidence for the attainability of time-reversed antiferromagnetic configurations by metamagnetic transitions in $DyPO_4$. *Phys. Rev. Lett.* **23**, 644–647 (1969).
111. Seyler, K. L. et al. Ligand-field helical luminescence in a 2D ferromagnetic insulator. *Nat. Phys.* **14**, 277–281 (2018).
112. Ferre, J. & Gehring, G. A. Linear optical birefringence of magnetic crystals. *Rep. Prog. Phys.* **47**, 513–611 (1984).
113. Nagaosa, N., Sinova, J., Onoda, S., MacDonald, A. H. & Ong, N. P. Anomalous Hall effect. *Rev. Mod. Phys.* **82**, 1539–1592 (2010).
114. Coey, J. M. D. in *Magnetism and Magnetic Materials* Ch. 10 (Cambridge Univ. Press, 2009).
115. Wang, Z. et al. Tunneling spin valves based on Fe_3GeTe_2/hBN/Fe_3GeTe_2 van der Waals heterostructures. *Nano Lett.* **18**, 4303–4308 (2018).
116. Arai, M. et al. Construction of van der Waals magnetic tunnel junction using ferromagnetic layered dichalcogenide. *Appl. Phys. Lett.* **107**, 103107 (2015).
117. Yamasaki, Y. et al. Exfoliation and van der Waals heterostructure assembly of intercalated ferromagnet $Cr_{1/3}TaS_2$. *2D Mater.* **4**, 041007 (2017).
118. Lohmann, M. et al. Probing magnetism in insulating $Cr_2Ge_2Te_6$ by induced anomalous Hall effect in Pt. *Nano Lett.* **19**, 2397–2403 (2019).
119. Gupta, V. et al. Current-induced torques in heterostructures of 2D van der Waals magnets. *Bull. Am. Phys. Soc. Abstr.* P15.009 (2019).
120. Moodera, J. S., Santos, T. S. & Nagahama, T. The phenomena of spin-filter tunnelling. *J. Phys. Condens. Matter* **19**, 165202 (2007).
121. Song, T. et al. Giant tunneling magnetoresistance in spin-filter van der Waals heterostructures. *Science* **360**, 1214–1218 (2018).
    The first demonstration of spin filtering and giant tunnel magnetoresistance using 2D CrI_3 as a tunnel barrier.
122. Kim, H. H. et al. One million percent tunnel magnetoresistance in a magnetic van der Waals heterostructure. *Nano Lett.* **18**, 4885–4890 (2018).
123. Kim, H. H. et al. Evolution of interlayer and intralayer magnetism in three atomically thin chromium trihalides. *Proc. Natl Acad. Sci. USA* **116**, 11131–11136 (2019).
124. Gould, C. et al. Tunneling anisotropic magnetoresistance: a spin-valve-like tunnel magnetoresistance using a single magnetic layer. *Phys. Rev. Lett.* **93**, 117203 (2004).
125. Cracknell, A. P. *Magnetism in Crystalline Materials: Applications of the Theory of Groups of Cambiant Symmetry* (ed. ten Haar, D.) Ch. 5 (Pergamon Press, 1975).
126. Coh, S., Vanderbilt, D., Malashevich, A. & Souza, I. Chern-Simons orbital magnetoelectric coupling in generic insulators. *Phys. Rev. B* **83**, 085108 (2011).
127. Wang, Z. et al. Electric-field control of magnetism in a few-layered van der Waals ferromagnetic

semiconductor. *Nat. Nanotechnol.* **13**, 554–559 (2018).

128. Jiang, S., Li, L., Wang, Z., Shan, J. & Mak, K. F. Spin tunnel field-effect transistors based on two-dimensional van der Waals heterostructures. *Nat. Electron.* **2**, 159–163 (2019).
129. Cardoso, C., Soriano, D., García-Martínez, N. A. & Fernández-Rossier, J. Van der Waals spin valves. *Phys. Rev. Lett.* **121**, 067701 (2018).
130. Ikeda, S. et al. Tunnel magnetoresistance of 604% at 300 K by suppression of Ta diffusion in CoFeB/MgO/CoFeB pseudo-spin-valves annealed at high temperature. *Appl. Phys. Lett.* **93**, 082508 (2008).
131. Lee, I. et al. Fundamental spin interactions underlying the magnetic anisotropy in the Kitaev ferromagnet CrI_3. Preprint at https://arxiv.org/abs/1902.00077 (2019).
132. Tate, M. W. et al. High dynamic range pixel array detector for scanning transmission electron microscopy. *Microsc. Microanal.* **22**, 237–249 (2016).
133. Saito, Y., Nojima, T. & Iwasa, Y. Highly crystalline 2D superconductors. *Nat. Rev. Mater.* **2**, 16094 (2016).
134. Zhou, B. T., Yuan, N. F. Q., Jiang, H.-L. & Law, K. T. Ising superconductivity and Majorana fermions in transition-metal dichalcogenides. *Phys. Rev. B* **93**, 180501 (2016).
135. Armitage, N. P., Mele, E. J. & Vishwanath, A. Weyl and Dirac semimetals in three-dimensional solids. *Rev. Mod. Phys.* **90**, 015001 (2018).

Acknowledgements

The authors acknowledge the support and encouragement of collaborators within the Cornell Centre for Materials Research, funded by the National Science Foundation Materials Research Science and Engineering Centers programme (DMR-1719875).

Author contributions

All authors co-wrote, discussed and commented on the manuscript.

Competing interests

The authors declare no competing interests.

Publisher’s note

Reviewer information

Nature Reviews Physics thanks W. Han and the other, anonymous, reviewer(s) for their contribution to the peer review of this work.